Synthesis of an Electroconductive Hydrogel in 3D Printing Formulation for Tissue Engineering

Åbo Akademi University

Faculty of Science and Engineering

Peter Odion Osazuwa

Master's program in Excellence in Analytical Chemistry

Degree project in Analytical Chemistry, 30 credits

Student Number: 2002159

Supervisor: Chunlin Xu (Åbo Akademi University)

Co-supervisors: Rose-Marie Latonen (Åbo Akademi University)

Xiaoju Wang (Åbo Akademi University)

Tarmo Tamm (University of Tartu)

June 2021

PREFACE

This master's thesis was done at Åbo Akademi University as a part of the Erasmus Mundus Joint Master's Degree program, Excellence in Analytical Chemistry.

The research presented in this thesis was carried out at the Laboratory of Molecular Science and Engineering and the Laboratory of Natural Materials Technology, Johan Gadolin Process Chemistry Centre, Åbo Akademi University, Turku/Åbo, Finland.

I would like to thank my supervisors for their excellent guidance and support throughout the research project and writing of this thesis. Special thanks to Prof. Chunlin Xu for the opportunity to explore this exciting field of study.

To Prof. Johan Bobacka, for his time, support, and invaluable comments which greatly improved the quality of this thesis, I am very grateful. Thank you, Dr. Tom Lindfors, for accepting the assignment of being my opponent.

Many thanks to Prof. Ivo Leito and Dr. Anu Teearu-Ojakäär for their endless guidance and assistance throughout my time in the EACH program.

To all my friends and colleagues, with whom I have shared many beautiful moments, thank you!

"One of the beautiful things about science is that it allows us to bumble along, getting it wrong time after time, and feel perfectly fine as long as we learn something each time"

-MARTIN A. SCHWARTZ, The Importance of Stupidity in Scientific Research

In Åbo, on a rainy day in May,

Peter Osazuwa

ABSTRACT

Osazuwa, Peter

Synthesis of an electroconductive hydrogel in 3D printing formulation for tissue engineering

Master's thesis

Laboratory of Molecular Science and Engineering and the Laboratory of Natural Materials Technology, Faculty of Science and Engineering, Åbo Akademi University, 2020 – 2021, 73 pages, 27 figures, 5 tables, 8 appendices

Supervisors

Prof. Chunlin Xu (ÅAU), Dr. Rose-Marie Latonen (ÅAU), Dr. Xiaoju Wang (ÅAU), and Prof. Tarmo Tamm (UT)

Keywords

Cellulose nanocrystal, colloidal stability, composite, electrically conducting polymer, electroconductive, galactoglucomannan, gelatin, hydrogel, polypyrrole, 3D printing

The progress made in tissue engineering to treat damage caused by disease and traumatic injury has been accelerated by innovations in bioengineering over the last few decades. The strategy of repairing and revitalizing damaged tissues has advanced from the use of tissue transplants to the use of functional scaffolds. Three-dimensional (3D) printing which utilizes hydrogel inks, is an ideal technique used to fabricate sophisticated and biomimetic hydrogel scaffolds capable of promoting new tissue morphogenesis via interaction with human cells. Electroconductive hydrogels have emerged as a significant tissue engineering scaffold due to their ability to maintain a distinct 3D structure, provide mechanical support for the cells in the engineered tissues, and their high electrical conductivity which is needed for the regeneration of electrically excitable tissues. However, the fabrication of electroconductive hydrogel scaffolds of high conductivity with high-quality 3D printing resolution remains a great challenge. In this research project, several methods were explored to fabricate high-quality 3D printable electroconductive hydrogel inks using cellulose nanocrystals (CNC), polypyrrole (PPy), and the photo cross-linkable gelatin methacryloyl (GelMA) and galactoglucomannan methacrylate (GGMMA). As revealed by the results, the hydrogel ink synthesized with CNC, PPy, and GGMMA possessed promising properties for high-quality 3D printing. The hydrogel ink was prepared by mixing the CNC/PPy with GGMMA. Analysis of the surface charge and particle size of CNC/PPy showed an improvement in the colloidal stability of the CNC/PPy composite at a CNC concentration of 1 wt% to 2 wt%. Also, after checking the conducting

properties of the CNC/PPy/GGMMA hydrogel inks with a two-point probe, a response was obtained on the multimeter for the hydrogel ink formulated with 1 wt% CNC and 0.2 M Py (CNC/PPy-3). Thus, the hydrogel fabricated with CNC/PPy-3 was used for further analysis. The incorporation of PPy was confirmed by the analysis of the hydrogel using Fourier transform infrared spectroscopy and UV-Vis spectroscopy. The electroconductivity of the hydrogel containing PPy was investigated using electrochemical impedance spectroscopy and compared to the control hydrogel without PPy. The impedance of the hydrogel decreased from 56.9 ± 1.9 kΩ for the control hydrogel to 43.3 ± 1.5 kΩ for the hydrogel containing PPy at 1 Hz. Likewise, the impedance of the hydrogel decreased from 113.4 ± 0.6 Ω for the control hydrogel to 79.9 ± 2.2 Ω for the hydrogel containing PPy at 1000 Hz. These results indicate the potential suitability of the hydrogel composed of CNC, PPy, and GGMMA for high-quality 3D printing and fabrication of tissue constructs for the regeneration of electrically excitable tissues.

TABLE OF CONTENTS

LIST OF SYMBOLS AND ABBREVIATIONS

AC	Alternating current
AcGGM	Acetylated galactoglucomannan
APS	Ammonium persulfate
ATR	Attenuated total reflectance
CNC	Cellulose nanocrystals
CNF	Cellulose nanofibers
CPE	Constant phase element
CV	Cyclic voltammetry
dECM	Decellularized extracellular matrix
DI	Deionized
DLS	Dynamic light scattering
E_{ac}	Alternating current potential
E_{dc}	Direct current potential
Eg	Band gap energy
EIS	Electrochemical impedance spectroscopy
FTIR	Fourier transform infrared
IR	Infrared
GelMA	Gelatin methacryloyl
GGM	Galactoglucomannan
GGMMA	Galactoglucomannan methacrylate
LAP	Lithium phenyl-2,4,6-trimethylbenzoylphosphinate
MA	Methacrylic anhydride
MCC	Microcrystalline cellulose

MMP	Matrix metalloproteinase
PEDOT	Poly(3,4-ethylenedioxythiophene)
PEDOT: PSS	Poly(3,4-ethylenedioxythiophene) doped with PSS
PPy	Polypyrrole
PVP	Polyvinylpyrrolidone
PSS	Polystyrene sulfonate
RGD	Arginine-glycine-aspartate
SD	Standard deviation
SEM	Scanning electron microscopy
TEM	Transmission electron microscopy
TEMPO	2,2,6,6-tetramethylpiperidine-1-oxyl
UV	Ultraviolet
UV-Vis	Ultraviolet-visible
ZP	Zeta potential
3D	Three-dimensional
α	Dispersion coefficient
σ	Single bond
π	Double bond
ϕ	Phase shift (angle)
ω	Angular frequency
$\|Z\|$	Impedance magnitude

1. INTRODUCTION

Disease and traumatic injury can cause damage to tissues in the human body which requires surgical intervention to facilitate their repair, replacement, or regeneration. Classical treatment strategies employ the transplant of tissues from one part of the patient's body to another (autotransplantation) or from a donor to the patient (allotransplantation). Despite the success of both strategies, some limitations exist. Autotransplantation is associated with a wide range of morbidity rates and various complications, such as infection, hematoma/seroma, nerve, and vascular injuries, chronic pain, and scars, while allotransplantation is limited by the problems of donor shortage and antibody-mediated rejection.[1,2] Three-dimensional (3D) printing, an advanced additive manufacturing technique, which can be used to fabricate complex, sophisticated, biomimetic tissue constructs, provides an alternative for the production of tissues to circumvent these limitations.[3] The 3D scaffolds provide the necessary support for cells to populate and function appropriately.

The 3D printing method utilizes biomaterials as bioinks for the fabrication of new scaffolds in combination with biological cues for tissue regeneration.[4] For example, natural polymers, such as collagen and gelatin, have been widely used as bioinks because they contain the tripeptide motif arginine-glycine-aspartate (RGD) which is important for cell adhesion, proliferation, and differentiation.[5,6] However, a single biomaterial in bioinks cannot usually satisfy all the conditions which are necessary to produce biomimetic tissue constructs. For example, the use of cytocompatible biopolymers such as gelatin is limited by their poor mechanical properties at physiological temperatures.[7] On the other hand, materials such as polyethylene glycol which allows the control of hydrogel mechanical modulus by varying molecular weight, lack the biological cues needed for cell adhesion and proliferation.[4,8] Hence, multicomponent bioinks composed of natural, synthetic, or hybrid biomaterials have been developed. Furthermore, the biomaterials should be carefully chosen to interact favorably with biological systems especially for cells of electrically excitable tissues such as neurons, fibroblasts, cardiomyocytes, and osteoblasts that require electrical stimuli to generate the necessary cellular responses.[9,10] Existing research recognizes the critical role played by electrical stimulation in tissue regeneration.[11,12] Thus, in addition to providing similar structure, mechanical, and biochemical properties to the native extracellular matrix, the successful engineering of these electrically responsive tissues requires scaffolds to be electroactive.[13]

In the past, various materials such as metal nanostructures (e.g. gold nanorod) and carbon-based materials (such as carbon nanotubes) have been used either purely or incorporated with other materials to form composites, to fabricate scaffolds.[14,15] These scaffolds were able to promote cell adhesion, migration, proliferation, and differentiation when used for electrically responsive cells. However, these materials have limitations, such as the high cost of gold that restricts their usage on a large scale and the potential cytotoxicity of carbon-based materials that limit their applications on implantable scaffolds.[14,15] To overcome this limitation, electrically conducting polymers such as polypyrrole (PPy),[16] polyaniline,[9] polythiophene,[17] and poly(3,4-ethylenedioxythiophene) (PEDOT)[18] have been used in biomedical applications due to their biocompatibility, conductivity, and reversible oxidation/reduction which are suitable properties for tissue engineering.[19] PPy is one of the most extensively explored electrically conductive polymers in tissue regeneration and it was reported that PPy-based materials show levels of immunogenicity that are similar to other biomaterials approved by the United States Food and Drug Administration.[20] The biocompatibility and toxicity of PPy have also been evaluated and it was reported that it did not have adverse effects on the cell cultures and animals tested.[21]

Hydrogels that form 3D cross-linked hydrated fibers have become the ideal material for developing scaffolds because of their similarity to the natural extracellular matrix of tissues which allows for the diffusion of nutrients, growth factors, and cellular waste.[22] However, they are characteristically non-conductive, which limits their application in modulating cell function for excitable cell types such as neurons, cardiomyocytes, and osteoblasts,[12,23] hence the emergence of electroconductive hydrogels. Electroconductive hydrogels belong to the general class of smart materials that utilize the inherent properties of electrically conductive polymers to design technologically relevant devices and systems.[22] Extensive research has shown that electrically conductive polymers can be used to fabricate electroconductive hydrogels. For example, Ketabat et al. synthesized an injectable conductive hydrogel using polypyrrole, alginate, and collagen for myocardial regeneration,[16] Wu et al. reported the fabrication of a conductive hydrogel using naturally-derived gelatin methacrylate and polyaniline which could support cell adhesion.[24] Also, Wang et al. reported the fabrication of a polypyrrole-grafted gelatin-based hydrogel with combined conductive, self-healing, and injectable properties.[25]

Due to the low mechanical properties of materials such as gelatin, it is necessary to combine them with other biomaterials to obtain multi-material hydrogel inks with improved properties.[8] The low mechanical property of gelatin is due to the breakdown of its secondary bonding

structure at temperatures above 35 °C.[7,8] This breakdown of the secondary bonding structure destroys the physical network of gelatin and thus, limits its application at physiologically relevant temperatures. Materials with good mechanical properties are important in tissue engineering because they should be able to sustain the mechanical forces they will experience when implanted at the defect site. Cellulose nanocrystal (CNC) is a form of nanocellulose that has several excellent characteristics such as high aspect ratio, easy surface functionalization, high mechanical strength, biocompatibility, biodegradability, and high availability at a relatively low cost, which makes it an ideal material for the reinforcing phase in a polymer matrix.[8,26,27] Previous studies have reported an enhancement in the mechanical properties of composite hydrogels after the incorporation of CNC.[8,28,29]

In addition to enhanced mechanical property and electroconductivity, the materials used for the synthesis of hydrogel inks need to be processed and formulated into printable inks for the fabrication of tissue scaffolds. The printability of bioinks is evaluated by the resolution and precision of the scaffold structures.[30] One important factor in the formulation of high-quality printable hydrogel inks is the integration of their components into a stable colloidal dispersion.[31] The behavior of particles in colloidal inks can be influenced by factors, such as particle size and surface chemistry, the tendency of aggregation, and ionic strength of the dispersion.[31] In the study by Zhang et al.[30], they reported an improved printing resolution due to the presence of colloidal lignin particles in the hydrogel ink which helped to stabilize the composite and prevented aggregation of particles. To meet the demands of the constantly evolving field of tissue engineering, it is vital to develop materials that satisfy the requirements of the hydrogel inks used for the engineering of electrically responsive tissues. This can be achieved using biocompatible materials with appropriate mechanical and electrical properties. Also, a suitable synthesis method aimed at good control of particle size and colloidal stability is vital.

Consequently, this project aims to develop a biocompatible, electroconductive, and 3D printable hybrid hydrogel for tissue engineering. The properties of the hydrogel inks are studied with different characterization techniques to assess their colloidal stability. The electroconductivity of the hydrogel is also characterized to evaluate its suitability for application in tissue engineering.

2. TISSUE ENGINEERING AND BIOMATERIALS

In tissue engineering, biomaterials serve as a temporary scaffold for the delivery and integration of cells and/or growth factors at the repair site. Scaffolds play a very crucial role in the development of new tissue morphogenesis by guiding the growth of cells seeded within them or helping cells migrate from surrounding tissues by communicating with them. They deliver cells to the desired sight in the patient's body, provide a space for new tissue formation, and provide sufficient structure and function (e.g., mechanical support) during the remodeling process.[32] An ideal tissue engineering scaffold must be capable of replicating the structure and function of the natural extracellular matrix of the body, and it should be degraded naturally during or shortly after the healing process.[33] In tissue engineering, hydrogel-based scaffolds have been extensively used due to their highly swollen three-dimensional (3D) environment. These scaffolds are very similar to soft tissues and allow for the diffusion of nutrients and growth factors through the elastic network which aids in the regeneration of damaged tissues. Hydrogels are characterized as either synthetic, natural, or hybrid (composite), based on the nature of their constituent polymers. In this thesis, several natural (GelMA, galactoglucomannan methacrylate, and cellulose nanocrystal) and synthetic (polypyrrole) polymers were explored in a hybrid form for the fabrication of the electroconductive hydrogel.

3. BIOPOLYMER-BASED BIOMATERIALS

Biopolymers are a class of natural polymers that are produced by living organisms. They are synthesized by enzymes that connect building blocks such as sugars, amino acids, or fatty acids to yield high molecular weight molecules. As biomaterials in tissue engineering, biopolymers offer diverse chemistries and help in the control of the structure and morphology of extracellular matrix systems. Another key advantage of biopolymers is their inherent biodegradability which helps to regulate the rate and extent of cell and tissue remodeling so that tissue regeneration occurs at a rate that matches the degradation of the scaffold.[34] Biopolymers that have been explored for tissue engineering applications are gelatin, collagen, and hyaluronate. These biopolymers are components of the extracellular matrix; hence they naturally interact with cells.[34] Also, due to the biocompatibility of wood-based biopolymers such as cellulose, hemicellulose, and lignin, they have attracted attention for application in tissue engineering.[32,35]

3.1. NANOCELLULOSE

Cellulose is the most abundant biopolymer on Earth, and it is the major component in lignocellulosic plant biomass.[36] Cellulose is a linear homo-polysaccharide comprising of D-glucose units connected by the β-1-4 glycosidic bond (**Figure 1**). Every other D-glucose unit is rotated 180° to its neighbor and two D-glucose units form a cellobiose unit. Each internal D-glucose unit has three hydroxyl groups (-OH): the -OH group at the C6 position is a primary alcohol, while the -OH groups at the C2 and C3 positions are secondary alcohols.[37] These hydroxyl groups are all potential sites for chemical modification of cellulose but the hydroxyl group at the C6 position is the most reactive.[38]

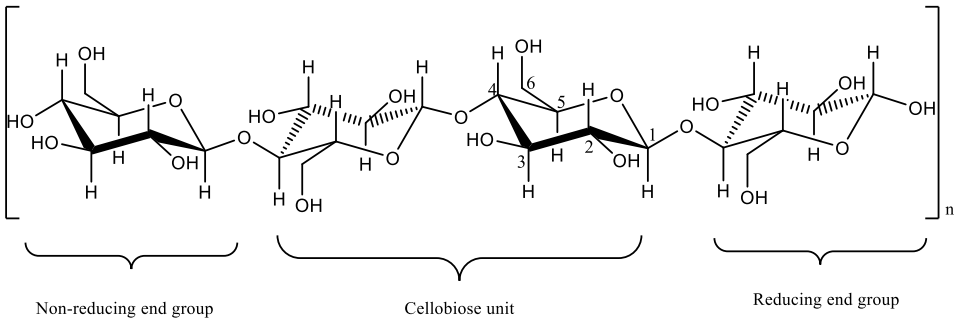

Figure 1. The molecular structure of a cellulose polymer.

As shown in **Figure 2,** to extract cellulose fibers, they must be detached from the other main components of the cell wall such as the hemicellulose and lignin. This is done via chemical or mechanical pulping into discreet fibers. The cellulose fibers can be defibrillated and/or hydrolyzed into smaller nanoscale entities known as nanocellulose, which occurs in the form of cellulose nanocrystals (CNCs) and cellulose nanofibers (CNFs).[39] Other forms of cellulose nanomaterials are algal cellulose, and bacterial cellulose.[40]

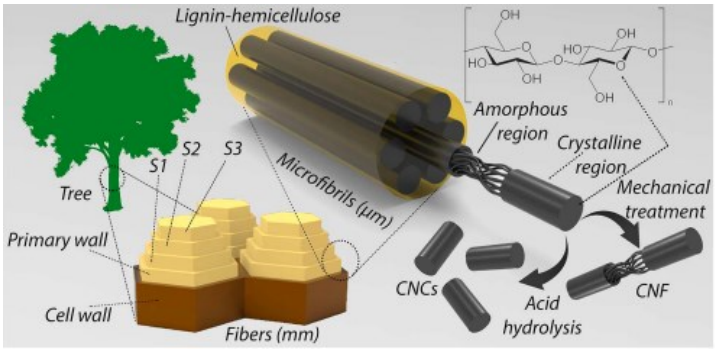

Figure 2. Schematic representation of the extraction of nanocellulose, in the form of CNFs and CNCs from cellulose fibers. Image is from "Current State of Applications of Nanocellulose in Flexible Energy and Electronic Devices," by Dias, O. A. T. *et al*., 2020, *Front. Chem.* 8 (Copyright: Frontiers Media S.A.).

Nanocellulose has received significant interest due to its mechanical and optical properties, biodegradability, availability, recyclability, renewability, and low coefficient of thermal expansion. Due to the presence of many hydroxyl groups within the nanocellulose structure as well as its high surface area and high aspect ratio, this enthralling biopolymer is a more attractive substrate for surface modification through various chemistries than traditional cellulose.[41] Another advantage of using renewable materials such as nanocellulose is that they can replace plastic and metal substrates in a wide range of applications and consequently reduce the pollutant deposits in the environment. Also, there has been rising concern about over-dependence on finite and diminishing non-renewable petroleum and metal resources. Thus, the use of advanced hybrid nanomaterials as a feedstock for next-generation materials such as hydrogels for tissue engineering has become a key principle of ecological sustainability.

3.1.1. CELLULOSE NANOCRYSTALS

Cellulose nanocrystal (CNC) is a form of cellulose nanomaterial with a typical length of 50-500 nm and a diameter of 3-10 nm that is primarily produced through acid hydrolysis of cellulosic fibers.[36] Compared to other forms of nanocellulose, CNCs have enhanced mechanical properties such as large surface area (~700 m^2/g), high Young's modulus (up to 140 GPa), high tensile strength, and stiffness.[37,42,43] Many other attractive features of CNC are biodegradability, biocompatibility, good colloidal stability, enriched surface-active groups, low cost, and abundance. Studies aimed at evaluating the biocompatibility and toxicity of CNC revealed that it did not affect the viability of colon epithelial cells and it showed minimal or no cytotoxicity in a cellular model of the intestinal epithelium.[44] These properties make CNC a promising functional nanomaterial for the fabrication of other hybrid nanostructures with enhanced properties. In recent years, CNCs have been widely explored as a reinforcement material to improve the mechanical properties of nano scaffold systems[45,46] and also used to direct the morphology and differentiation of skeletal muscle cells.[47]

The production of cellulose nanomaterials from plant biomass is important because cellulose is stronger than steel when density difference is factored in and it is comparable to carbon nanotubes. Also, the crystalline cellulose tensile strength and modulus are approximately 10 and 100 times that of wood, respectively.[36] CNC is primarily produced from cellulosic fibers through acid hydrolysis. Through controlled acid hydrolysis, crystallites can be isolated from natural cellulose by selectively hydrolyzing the water-accessible crystal defects and disordered regions.[36,37,48,49]

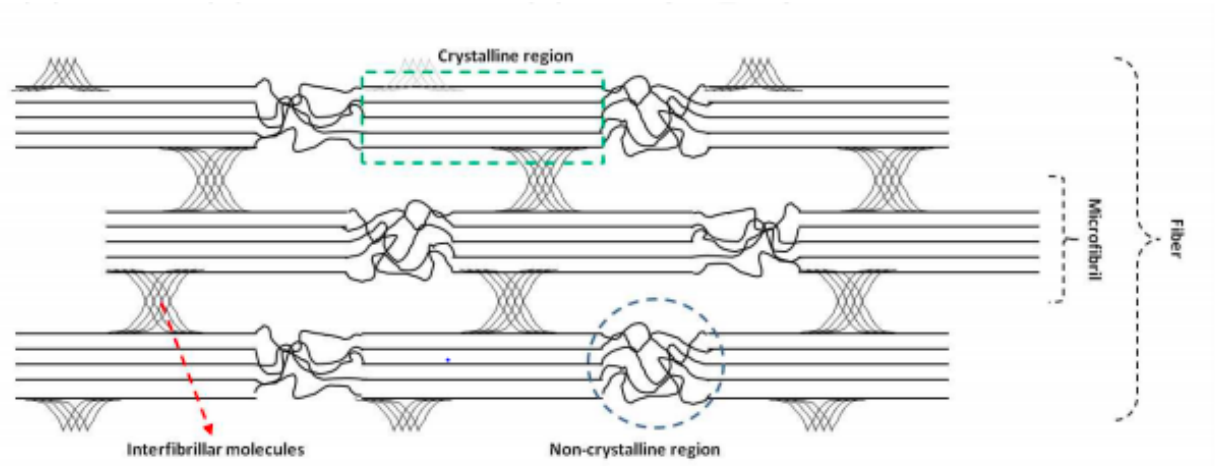

Figure 3. Schematic representation of a cellulose fiber showing the crystalline and non-crystalline regions. Acid hydrolysis removes the non-crystalline regions and only crystalline parts (CNC) will remain. Image is from "Crystalline Nanocellulose — Preparation, Modification, and Properties," by Börjesson, M. & Westman, G., 2015, *Cellul. - Fundam. Asp. Curr. Trends* (Copyright: IntechOpen).

In the early stage of hydrolysis, the acid diffuses into the non-crystalline parts of the cellulose fiber and hydrolyzes the glycosidic bonds. This is followed by hydrolysis at the reducing end group and the surface of the cellulose nanocrystals.[37] The hydrolysis of the reducing end groups and the surface of the nanocrystals will make the nanocrystals charged depending on the type of acid that is used. Although acids such as hydrochloric acid and hydrobromic acid can be used for hydrolysis, sulphuric acid is commonly used because of the formation of sulfate half-ester groups on the crystalline surface (**Figure 4**) that impart electrostatic stability to CNC which promotes stable colloidal dispersion.[36,37]

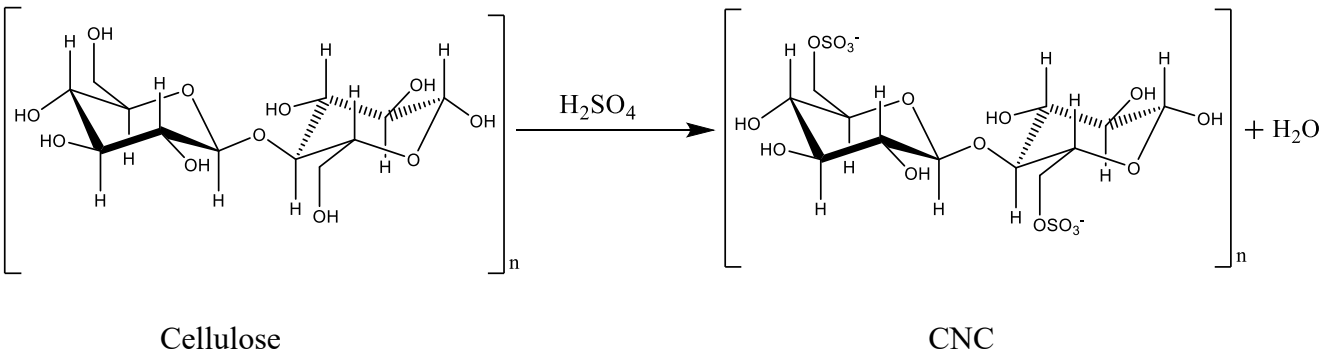

Figure 4. Schematic representation of the production of CNC by sulphuric acid hydrolysis.

Acid type and concentration, reaction time, and reaction temperature are some of the most important parameters for controlling the acid hydrolysis of cellulose fibers. A reaction time that is too long will hydrolyze the cellulose crystals completely and a reaction time that is too

short will give a high degree of polymerization due to large undispersed fibers.[37] The sulphuric acid hydrolysis reaction has been optimized by several researchers and the generally adopted way to produce CNC is by using a 64 wt% sulphuric acid solution at 45 °C for 45 to 60 min with constant stirring. After hydrolysis, centrifugation, and purification through dialysis, small crystalline rod-like particles will be yielded in an aqueous suspension.[36,37,40] CNCs have been hydrolyzed from various cellulose sources such as microcrystalline cellulose (MCC),[50] cotton,[42] rice straw,[51] bacterial cellulose,[52] wood,[53] banana fibers,[54] sugarcane bagasse,[55] rejected fibers,[55] and grass fibers.[56] CNC was used in this thesis due to its excellent mechanical properties which makes it a suitable reinforcement material in the hydrogel matrix. Additionally, the surface charge of CNC will help to increase the electrostatic repulsion in the composite and promote the colloidal stability of the particles in the composite.

3.1.2. CELLULOSE NANOFIBRES

Cellulose nanofibres (CNFs) consist of a bundle of individual nanofibrils entangled together and comprised of alternating amorphous and crystalline cellulose domains.[57] The leading method of CNF isolation is the disintegration of the cell wall matrix through mechanical shear (grinding, high-pressure fluidizers, and high-pressure homogenizer) to release microfibrils. To cut down up to 98 % of the energy consumed during the mechanical disintegration, standard pretreatment processes such as carboxymethylation or 2,2,6,6-tetramethylpiperidine-1-oxyl (TEMPO)-mediated oxidation have been applied before the defibrillation. The pre-treatment is separated into two categories: enzymatic (e.g., TEMPO oxidation) or mild acid hydrolysis and introduction of electrostatic repulsion between the fibers through chemical modification of the fibrils to generate anionic surface charges.[57] Other pretreatment techniques are phosphorylation and periodate oxidation but the central theme of these processes are similar to TEMPO oxidation: addition of charge on the microfibril surface to facilitate the detachment of microfibrils from one another into CNFs.[58]

CNFs offer several benefits for the preparation of nanomaterials. Their high aspect ratio allows easy preparation of nanomaterials due to the robust network formed by vast entanglement and short-range interactions. They are also generally used for composite reinforcement because the crystalline part of cellulose has a high stiffness (modulus of ca. 150 GPa and tensile strength of ca. 10 GPa).[59] Due to its fascinating properties, several applications of CNF have been

proposed in energy storage and harvesting, sensing devices, electronic devices, water treatment and air filtration, and biomedical applications.[59]

3.2. HEMICELLULOSE

Hemicelluloses are a group of heterogeneous plant cell wall polysaccharides and the world's second most abundant renewable biopolymers after cellulose in lignocellulosic materials.[60] They can be extracted by water or aqueous alkali from plant tissue, and they comprise a wide variety of monosaccharides including xylose, arabinose, glucose, galactose, mannose, fucose, glucuronic acid, and galacturonic acid, depending upon the source.[60] Hemicelluloses in hardwood are glucuronoxylan (most abundant in hardwood), glucomannan, and xyloglucan while softwood hemicelluloses are galactoglucomannan (most abundant in softwood), arabinoglucuronoxylan, and arabinogalactan.[60]

Due to the biocompatibility, biodegradability, and environmentally friendly properties, hemicellulose has attracted much attention for applications in different areas such as biofilms, food packaging, and biomedical applications.[61] For example, electrically conductive hemicellulose hydrogels have been fabricated via cross-linking O-acetyl-galactoglucomannan with epichlorohydrin in the presence of conductive aniline pentamer at ambient temperature. The formed hydrogel had a macroporous structure, controllable conductivity, tunable swelling behavior, and good mechanical properties, which has great potentials for biomedical applications such as tissue engineering.[62]

3.2.1. GALACTOGLUCOMANNAN

The major hemicelluloses in softwood are acetylated galactoglucomannan (AcGGM) shown in **Figure 5**. The main chain is believed to be linear or slightly branched and consists of a backbone of (1 → 4)-linked β-D-glucopyranose and β-D-mannopyranose units with α-(1 → 6)-D-galactopyranose. A vital structural feature is the hydroxyl groups at the C2 and C3 positions in the main chain units which are partially substituted by *O*-acetyl groups, with an average of one group per 3 to 4 hexose units containing this substitution.[63] AcGGM has an approximate degree of polymerization between 100 and 150, which is equivalent to a molecular weight of around 16,000 to 24,000 Da.[63]

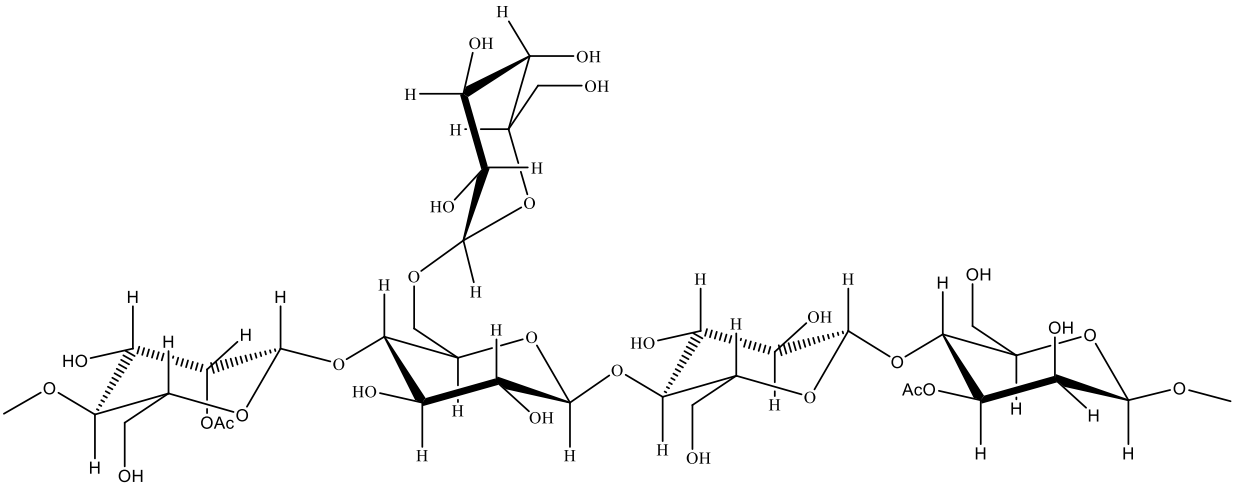

Figure 5. Structure of O-acetyl-galactoglucomannan (AcGGM).

Galactoglucomannans are easily depolymerized by acids, especially the bonds between galactose and the main chain while the acetyl groups are much more easily cleaved by alkali and acid.[60] Due to the presence of a high amount of hydroxyl groups, AcGGM can react with acids, acid anhydrides, acid chlorides, etc to form modified products for applications as an oxygen barrier, water-resistant coatings, and hydrogels.[61]

3.3. PHOTOPOLYMERIZABLE BIOPOLYMERS

Photopolymerizable biomaterials are commonly used in tissue engineering because of the spatiotemporal control provided by photoinitiated photopolymerizations.[64] Photopolymerization reaction is fast and controllable, and requires low energy input, compared to a traditional radical polymerization.[65]

A key factor in the development of photopolymerizable materials for 3D printing is to incorporate photoreactive moieties such as methacrylate, acrylate, or thiol-ene groups. For example, biopolymers such as gelatin, collagen, hyaluronic acid, decellularized extracellular matrix (dECM), alginate, and galactoglucomannan have been made photopolymerizable via the incorporation of photoreactive moieties such as (meth)acrylate groups.[64,66,67] Although there are several types of photopolymerization mechanisms such as orthogonal step-growth polymerization, two-photon polymerization, and ionic photopolymerization, the free-radical chain-growth polymerization is the most widely used.

3.3.1. PHOTOINDUCED FREE-RADICAL CHAIN GROWTH POLYMERIZATION

Most photoreactive biomaterials undergo photoinduced free-radical chain-growth polymerization to form a cross-linked hydrogel. It involves the decomposition of photoinitiators upon light exposure to form radicals which serve as kinetic-chain carriers by attacking nearby free monomers to initiate chain-growth polymerization. The polymerization is defined by three distinct stages: initiation, propagation, and termination. In the initiation stage, the light (usually UV irradiation) strikes the photo-initiator and cleaves it into two free-radicals via bond cleavage at sites such as C-C, C-Cl, C-O, or C-S bonds.[64] Thereafter, one or both free radicals initiate the polymerization by reacting with the monomer to form a radical. The newly radicalized monomer can react with another monomer, and this continues to propagate in a chain-like fashion. The propagation of the polymer chain continues until a termination reaction occurs.[64] Lithium phenyl-2,4,6-trimethylbenzoylphosphinate (LAP), and 2-hydroxy-4′-(2-hydroxyethoxy)-2-methylpropiophenone (Irgacure-2959) are photoinitiators that are commonly used in photopolymerization. LAP has an absorbance maximum at around 375 nm and significant absorbance at 365 nm. The absorbance of Irgacure-2959 is around 270 nm but this is phototoxic and mutagenic for cellular encapsulation since DNA absorbs light at 260 nm and proteins absorb light at 280 nm.[68] Hence, for applications involving cells, the light source is filtered to allow light at 365 nm. At 365 nm, the molecular coefficient of Irgacure-2959 is very low and it lags off almost completely before 370 nm. Thus, the utilization of Irgacure-2959 for photopolymerizations performed at 365 nm or longer wavelengths is limited.[68]

During photopolymerization, oxygen impurities can react with free radicals and impede their propagation. This may increase the time required for crosslinking (UV irradiation exposure time) and affect printing resolution.[64] Since oxygen can diffuse into biomaterials over time, they are often deaerated with nitrogen gas before photopolymerization to minimize the impact of oxygen.

3.3.2. GALACTOGLUCOMANNAN METHACRYLATE

Galactoglucomannan (GGM) consists of a high amount of free hydroxyl groups that can be functionalized with methacrylate groups to form galactoglucomannan methacrylate (GGMMA). A green approach for synthesizing GGMMA by reacting GGM with methacrylic

anhydride (MA) in an aqueous solution under a mild alkaline condition at 50 °C has been reported (**Figure 6**).[67]

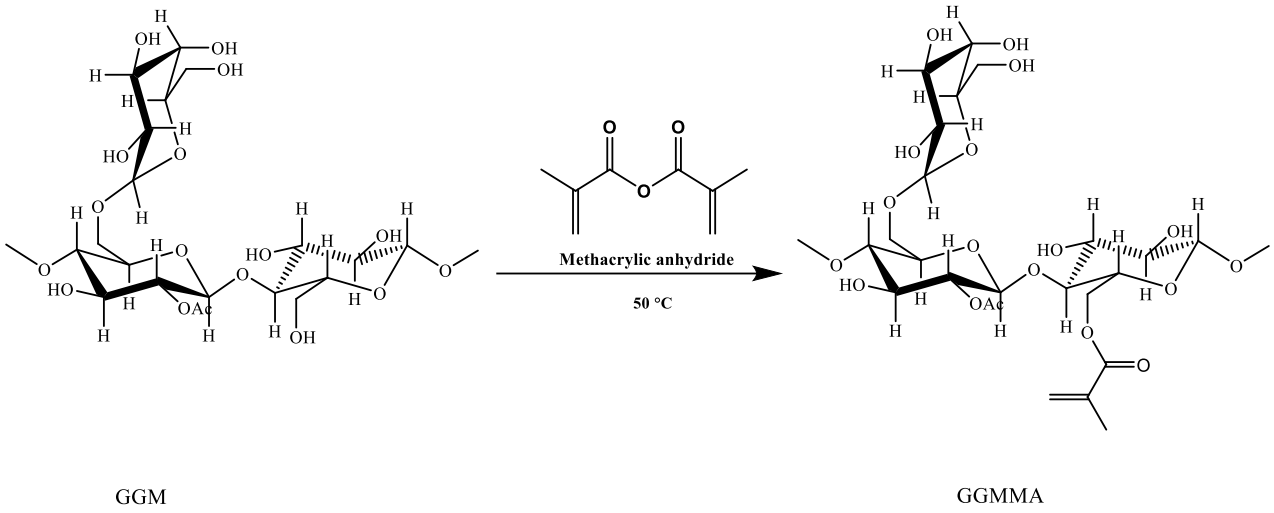

Figure 6. Schematic representation of the synthesis of GGMMA.

It was also reported that a hydrogel ink that consists of GGMMA/CNF showed good mechanical properties and cytocompatibility.[67] Hence, the biocompatible and biodegradable properties of GGMMA make it a suitable biopolymer for application in tissue engineering. Due to the presence of the photoreactive moiety (MA) in GGMMA, it was used in one of the methods in this thesis to form the hydrogel.

3.3.3. GELATIN METHACRYLOYL

Gelatin is a natural hydrophilic polymer produced from hydrolysis and denaturation of collagen under high temperature and it is biocompatible, soluble in aqueous and organic solvents, biodegradable, and unlike collagen, it is non-immunogenic. Furthermore, gelatin possesses the arginine-glycine-aspartate (RGD) peptide sequence which facilitates certain cell adhesion, proliferation, and differentiation. It also possesses a matrix metalloproteinase (MMP) degradation sequence which promotes cell enzymatic degradation.[69] Due to the presence of active groups (-OH, -COOH, -NH_2, -SH) on the side chains of gelatin, it can be modified with specific groups to improve its properties for various applications. The most used method of functionalizing gelatin is the synthesis of gelatin methacryloyl (GelMa) which is widely used in tissue engineering.

GelMA is produced through the reaction of gelatin with MA via one-pot synthesis to conjugate methacryloyl groups predominantly to amine groups and less so to the hydroxyl groups present along the gelatin backbone and this method was first reported in the year 2000 by Van Den Bulcke et al.[70] (**Figure 7**). The reaction typically takes place in phosphate buffer (pH = 7.4) at 50 °C.

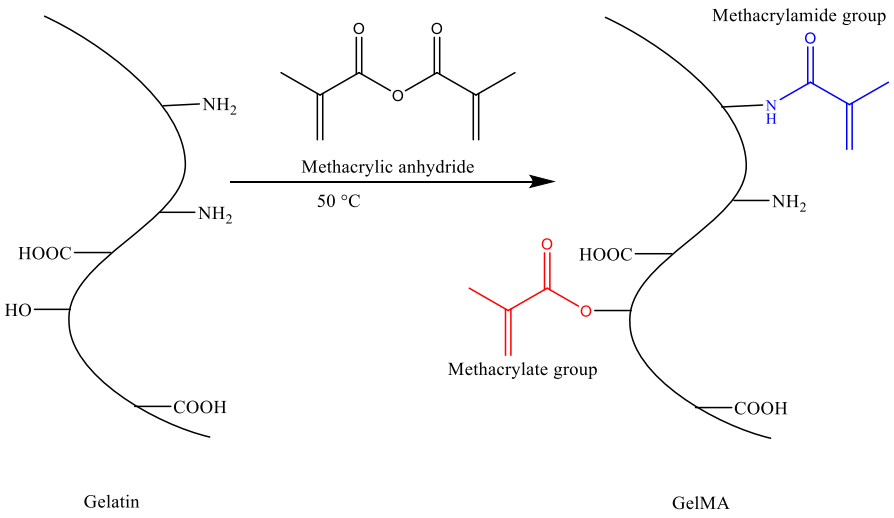

Figure 7. Schematic representation of the synthesis of amphoteric GelMA showing the methacrylate group (red color) and methacrylamide group (blue color).

Different degrees of methacryloyl substitution can be achieved in GelMA by changing the amount of MA added to the reaction mixture, which produces GelMA with distinct mechanical properties.[71] The chemical modification of gelatin by MA involves less than 5 % of the amino acid residues in the molar ratio, which implies that the RGD motifs and MMP-degradable motifs will not be drastically influenced.[70,71] Besides, the RGD motifs do not contain groups that will react with MA, which ensures the retention of good cell adhesive properties of GelMA.[71,72]

GelMA crosslinks immediately under UV light when a photoinitiator is added via a photoinduced free-radical polymerization to form GelMA hydrogels which have excellent thermostability.[69] Common photoinitiators used for photocrosslinking GelMa are 2,20-azobis[2-methyl-*N*-(2-hydroxyethyl)propionamide] (VA-086), lithium phenyl-2,4,6-trimethylbenzoylphosphinate (LAP), and 2-hydroxy-4′-(2-hydroxyethoxy)-2-methylpropiophenone (Irgacure-2959). GelMA hydrogels have been widely used for various biomedical applications due to their suitable biological properties and tunable physical

characteristics. The main disadvantage of GelMA is its mechanical robustness; as a protein biopolymer, it is susceptible to hydrolytic and enzymatic degradation, and it has a relatively narrow stiffness range.[64] To overcome this, GelMA is commonly implemented in composite biomaterials. Due to the presence of the photoreactive moiety (MA) in GelMA, it was used in one of the methods in this thesis to form the hydrogel.

4. ELECTRICALLY CONDUCTING POLYMERS

Electrically conducting polymers are a class of a new generation of smart biomaterials that permit the transfer of electrical, electrochemical, and electromechanical stimulation to cells.[73] The modern development of conductive polymers was triggered by the observation of Heeger, MacDiarmid, and Shirakawa, who were jointly awarded the Nobel Prize in Chemistry in the year 2000 for the discovery and development of conductive polymers. They reported that the conductivity of polyacetylene, a polymer that is normally only semiconducting at best, increases by 10 orders of magnitude when it is oxidized using iodine vapor.[74] Since then, conductive polymers such as polypyrrole, polyaniline, polythiophene, and poly(3,4-ethylenedioxythiophene) which exhibit excellent electrical and optical properties have been explored in many applications including energy storage devices, actuators, light-emitting diodes, etc. The molecular structures for the listed conjugated polymers are shown in **Figure 8**. After the pioneering work of Wong et al.[75] who seeded mammalian cells on the conductive films based on polypyrrole, more conductive polymers have been explored for tissue engineering applications.[76–78]

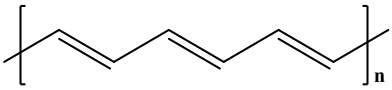

Trans-polyacetylene

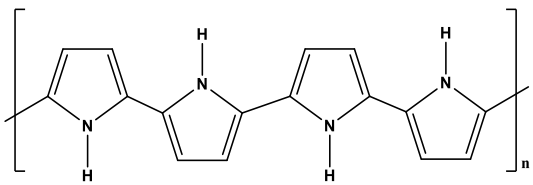

Polypyrrole

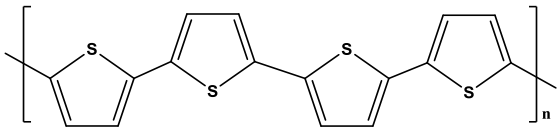

Polythiophene

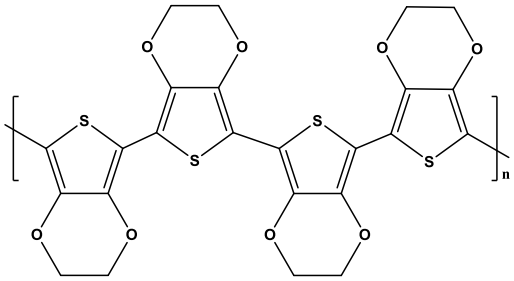

Poly(3,4-ethylenedioxythiophene)

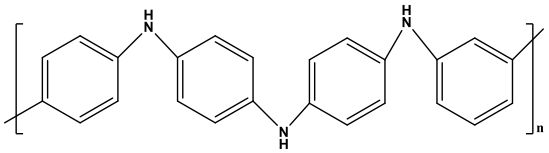

Polyaniline

Figure 8. Molecular structures of some common conductive polymers in their undoped state.

Electrically conductive polymers have a conjugated bond structure that contains localized carbon-carbon single bonds (σ) and less localized carbon-carbon double bonds (π) (**Figure 9**). The overlapping *p*-orbitals in the series of π-bonds allow for electron delocalization i.e. they do not belong to a specific monomer, but the whole π-electron network. Thus, it allows charge transport along the polymer backbone (intra-chain charge transfer) or in between polymer chains (inter-chain charge transfer).[73,79]

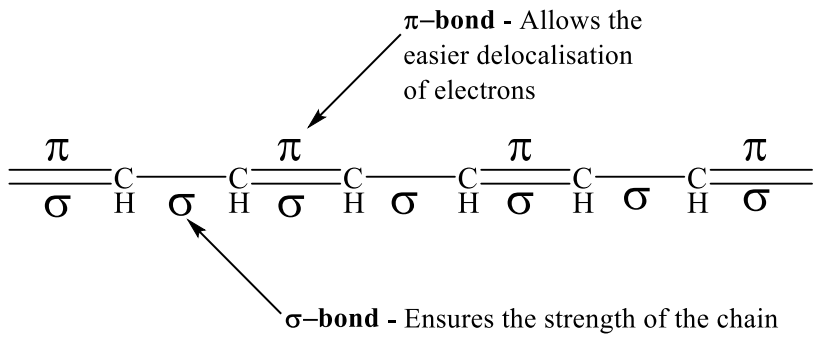

Figure 9. A simplified scheme of a conjugated backbone: a chain containing alternating single and double bonds.

In electrically conducting polymers, the unsaturated bonds (π-bonds) are shorter than the saturated bonds (σ-bonds) and the alternation of the π-bonds and σ-bonds (bond length alternation) in the polymer backbone results in the band gap or Peierls gap (E_g).[80] All states below the gap are occupied and form the π-band (valence band), and the states above the gap are empty and form the π*-band (conduction band). As shown in **Figure 10**, when the valence band overlaps the conduction band, the valence electrons are free to move and spread in the conduction band and this is an intrinsic characteristic of metallic conductors. Semiconductors possess small E_g that electrons can cross upon excitation to reach the conduction band. In the case of insulators, the band gap is too large to be crossed by electrons, hence they do not conduct electricity.[81]

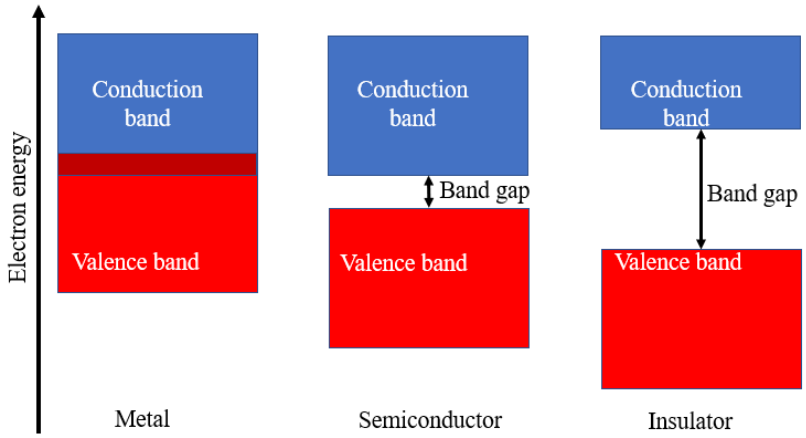

Figure 10. Schematic representation of metals, semiconductors, and insulators in terms of the band gap (E_g).

Pristine electrically conducting polymers are essentially insulators because the energy gap separating the valence and conduction band is too large for the valence electrons to move and propagate in the conduction band. It is also believed that there is a distinct structural and morphological disorder in the polymer matrix that delays charge transport along the polymer chain.[81] The key to the conductivity of electrically conducting polymers is doping.[73,82] The doping of a conducting polymer involves the partial oxidation (p-doping) or reduction (n-doping) of the polymer. This can be accomplished either chemically or electrochemically. During doping, the twisted benzoid-like structure is transformed into a quinoid-like structure thereby reducing the structural lattice distortion. Doping also introduces charge carriers to the polymer chain in the form of polarons and bipolarons. The polarons and bipolarons create sublevels between the valence and conduction bands which make it possible for the electrons to move.[81] The high conductivity of the doped conjugated polymers is due to the increase in the number of free charge carriers, and the mobility of electrons as new electronic bands are

formed between the conduction and valence bands. The structure of positively charged polaron and bipolaron are shown in **Figure 11**.

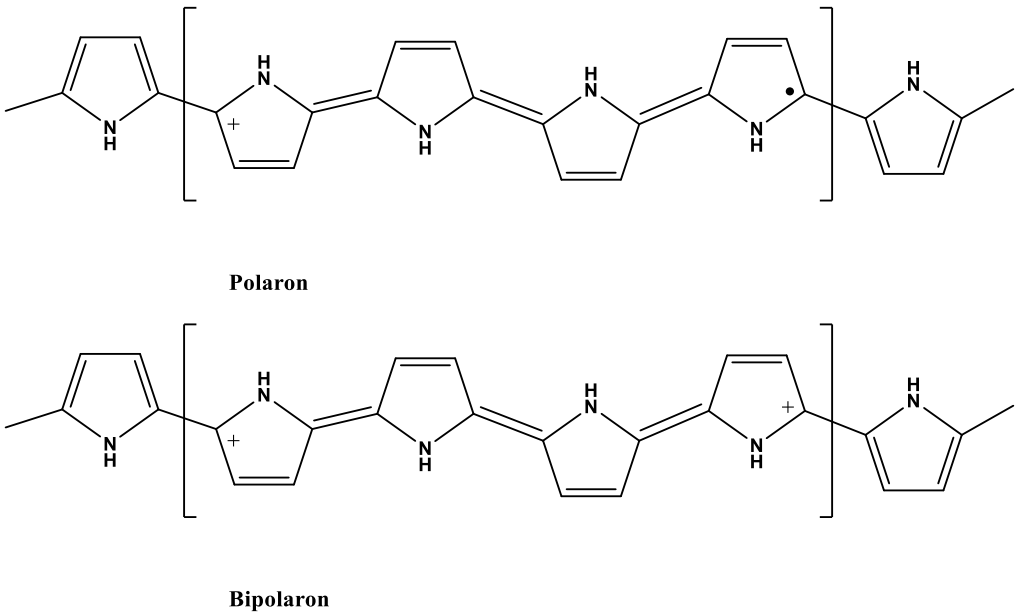

Figure 11. The quinoid structure of polaron and bipolaron in polypyrrole.

Counterions or dopants neutralize the charge introduced through oxidation (p-doping) or reduction (n-doping) and stabilize the polymer backbone.[73] Different polysaccharides anionic templates have successfully been applied as dopant anions for electrically conducting polymers. For example, PPy has been successfully synthesized via situ polymerization of pyrrole monomer in presence of CNC[83,84] and tannic acid[85] as dopants. Due to this unique property of electrically conducting polymers, it is desirable to incorporate them inside bulk hydrogels in a superstructure and ordered fashion to allow inter and intra-chain charge transfer throughout the hydrogel.

4.1. POLYPYRROLE

Polypyrrole (PPy) is one of the most widely studied electrically conducting polymers for biomedical applications due to its high conductivity, biocompatibility, and easy synthesis.[86,87] Various studies have reported the combination of PPy with biopolymers to make hybrid biomaterials for tissue engineering. For example, Zhou et al.[85] reported the fabrication of a soft conducting PPy hydrogel cross-linked and doped with tannic acid for spinal cord injury repair. Also, Wright et al.[86] synthesized a conductive composite of PPy and alginate which was suitable for 3D extrusion printing and facilitated the proliferation of PC 12 neuronal cells. In another study, Yang et al.[88] fabricated a conductive PPy/alginate hydrogel which enhanced the cell adhesion and growth of human bone marrow-derived mesenchymal stem cells. PPy is

generally synthesized by chemical or electrochemical methods. Electrochemical synthesis results in the formation of thin films while chemical synthesis is used when large quantities of material are required, and this method was adopted in this thesis.

Although the mechanism of PPy synthesis by the chemical method is debatable, the most widely accepted polymerization mechanism is the coupling between radical cations.[89] As the first step, pyrrole is oxidized to give a radical cation. This is followed by dimerization because of radical-radical coupling to form a positively charged dimer. The positively charged dimer is then deprotonated and reoxidized to form a dimer radical cation. This is followed by coupling between dimer radical cations (and later between oligomers), deprotonation, and rearomatization (**Figure 12**).[89,90] This mechanism was confirmed by Heinze et al.[74] who unambiguously showed that the consecutive oligomerization of conductive polymers starts in solution and preferably takes place through successive dimerization steps leading from a dimer to a tetramer and then to an octameric coupling product. By this repeated process, the chains grow and finally lead to the polymer.

Pyrrole oxidation

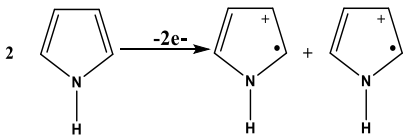

Formation of dimer

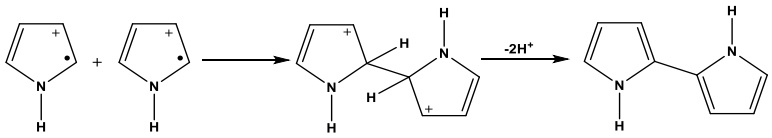

Oxidation, coupling and re-aromatization

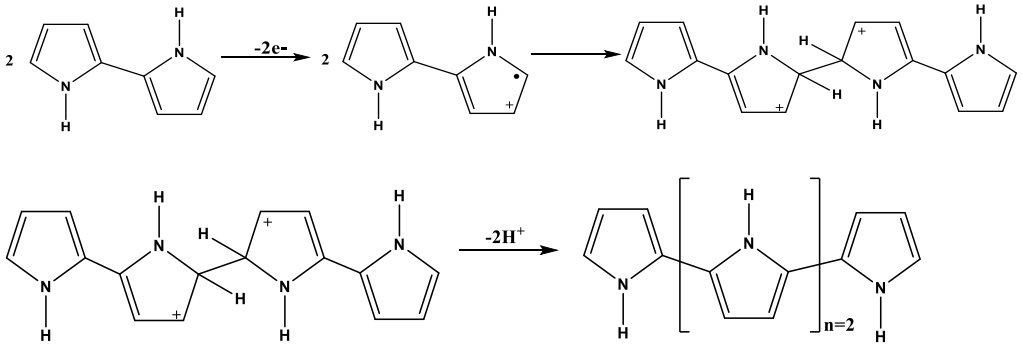

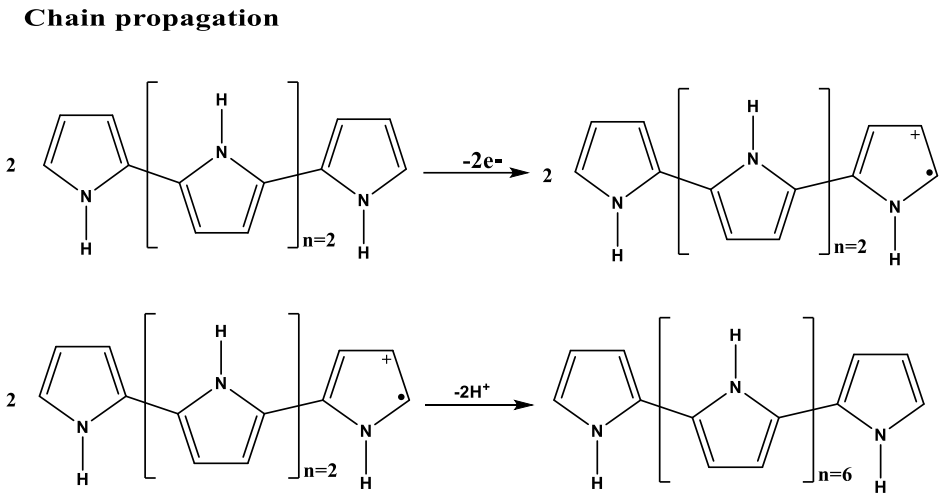

Figure 12. Mechanism of chemical synthesis of Polypyrrole.

Pyrrole is oxidized by compounds such as $FeCl_3$, $FeCl_3 \cdot 6H_2O$, and $(NH_4)_2S_2O_8$ (APS), hence they are usually used in its chemical polymerization. The influence of the oxidants and oxidant to monomer ratio in the chemical polymerization of PPy in aqueous solutions has been investigated. Yussuf et al. compared the performance of $FeCl_3$ and APS at room temperature and reported a higher conductivity when $FeCl_3$ was used.[91] Also, Yussuf et al.[91] and Armes[92] have shown that the optimal mole ratio of $FeCl_3$/pyrrole is approximately two (2). Furthermore, APS has been utilized in other studies involving composites of PPy, and acceptable levels of conductivity were reported.[25,93] Studies have shown that polymerization is accompanied by unwanted side reactions such as overoxidation which affects the properties of the polymer.[94,95] In a study, it was reported that overoxidation occurs mainly at the beginning of the chemical polymerization and is boosted by low oxidant concentration.[94] The authors concluded that a higher oxidant concentration will result in higher conductivity of the polymer. In another study by Wu et al.[95] where they performed an in-situ polymerization of PPy in a solution of CNC and polyvinylpyrrolidone, they reported that overoxidation was caused by an extended period of polymerization. In their study, they reported that the PPy growth on the surface of CNC reached a conducting threshold at 3 h and it plateaued after 6 h where it remained constant for the next 10 h after which it rapidly decreased. These studies suggest that factors such as polymerization time, oxidant type, oxidant concentration, and oxidant to monomer ratio influence the final product of polymerization. PPy was used in this thesis to make the hydrogel electroconductive.

5. CHARACTERIZATION TECHNIQUES

5.1. ZETA POTENTIAL

Zeta potential (*z*-potential) also known as electrokinetic potential is a measure of the charge on the surface of particles and gives information about the charge stability of colloidal nanoparticles.[96] It depends on factors such as strength and valency of the ions, and pH of the medium. The measurement of *z*-potential is based on the electrophoretic mobility of the particles after the application of an electric field to the sample. Electrophoretic mobility is the degree to which the particles alter their movement proportional to the externally applied electrical field.[97] *Z*-potential can be resolved from the measured electrophoretic mobility of the particle, based on the Henry equation below:

$$U_e = 2\varepsilon z\, f(Ka) / 3\eta \qquad \textbf{Equation 1}$$

where U_e is electrophoretic mobility, ε is dielectric constant (i.e the relative permittivity of the sample), z is zeta-potential, $f(Ka)$ is Henry's function (Smoluchowski approximation is usually applied where $f(Ka)$ is equal to 1.5), and η is the viscosity of the solvent.[97] Z-potential of ± 30 mV indicates particle stability, where values greater than +30 mV or less than -30 mV infers stability or an ability to resist the aggregation of particles.[98,99] Zeta-potential was used in this thesis to analyze the surface charge and assess the colloidal stability of the composites and hydrogel inks.

5.2. DYNAMIC LIGHT SCATTERING

Dynamic light scattering (DLS) is a simple and commonly used method to estimate particle size in a dispersed medium. DLS measures light scattered from a laser that passes through a solution of nanoparticles undergoing Brownian motion. The motion of the particles which is driven by gradients in the particle concentration is described by the translational diffusion coefficient.[100] This is important in DLS analysis because larger particles will move more slowly than smaller particles and scatter more light. The hydrodynamic diameter of the particles can be calculated from the time dependence of the scattering intensity measurements based on the Stokes-Einstein equation (**Equation 2**).[101]

$$D = KT/3\pi\eta D_t \qquad \textbf{Equation 2}$$

where D is the hydrodynamic diameter (reported as the mean particle size), K is Boltzmann's constant ($J \cdot K^{-1}$), T is the absolute temperature (K), η is the viscosity of the solvent (Pa·s) and D_t is the translational diffusion coefficient (m^2/s). The hydrodynamic diameter is the diameter of a hypothetical sphere that diffuses at the same rate as the measured particle.[96] Although the hydrodynamic diameter is slightly larger than the "physical" particle, the results of DLS measurements for unaggregated colloidal solutions are comparable to particle size obtained with transmission electron microscopy.

While DLS measurement leads to acceptably accurate results for monodisperse nanoparticles, it is unable to differentiate between nanoparticles with slight differences in diameter or to precisely resolve polydisperse samples.[97,102] This is because it measures the intensity of the scattered light to the sixth power of the particle diameter, thus a population of large particles in the sample can skew the results.[103] DLS works best with homogenous particles in a transparent solvent which ensures the stability of the sample in suspension.[104] Hence, the results of DLS measurements for polydisperse samples due to particle aggregation are not reliable. DLS was used in this thesis to analyze the size of the particles to identify possible particle aggregation.

5.3. SCANNING ELECTRON MICROSCOPY

Scanning electron microscopy (SEM) is a high-resolution imaging technique that is usually used in the investigation of surface morphology (texture), size distribution, aggregation, and chemical composition of materials.[96,98] It is vital in hydrogel characterization because during cell culture, the microstructure of the hydrogels, such as the pore size and fiber arrangement, influences the behaviors of the cells, such as their growth, migration, proliferation, and alignment which consequently affects the processes of vascularization and osteogenesis.[105] If the hydrogels show good porosity, the growth of the cells would not be inhibited, since the cells could readily spread and proliferate following their encapsulation within the hydrogels.

SEM operates by generating a beam of electrons in a vacuum. The beam is focused by electromagnetic lenses within a column and directed towards the sample. The interaction of the electron beam with the sample causes the ionization of the sample (ejection of electrons from the atoms within the sample to produce secondary electrons), and reflection (back-scattering) of the beam electrons from the sample surface to produce the backscattered electrons. With the aid of a secondary electron detector, the crystal shape and surface morphology of the materials can be visualized.[98] SEM can be equipped with an energy-dispersive X-ray spectrometer (EDS)

for elemental analysis of materials. The EDS detects and identifies the X-rays that are emitted by the atoms on the surface layer of the material being analyzed.[106] The X-rays are emitted when the vacancy in the inner electron shell (due to the production of the secondary electrons) is filled by an electron from an outer shell. Elements emit X-ray photons with characteristic energies and the EDS measures the energy of each emitted photon to identify the elements in the material. The abundance of the emitted photons also gives information about the abundance of the specific elements on the sample. SEM was used in this thesis to analyze the surface and cross-sectional morphology of the hydrogel.

5.4. TRANSMISSION ELECTRON MICROSCOPY

Transmission electron microscopy (TEM) is a common technique for characterizing the shape and size of nanoparticles at high magnification.[98] It is the most used technique for the characterization of nanoparticles because of the high spatial resolution as compared with SEM.[40] In TEM, the focused electron beam passes through a series of electromagnetic lenses and illuminates the whole area of the sample. The electron is collected below the sample and projected onto a phosphorescent screen. Thus, the sample should be very thin to allow the electrons to pass through it.[98] One limitation of TEM is that the sample and substrates (pedestal and grid used in sample preparation) are typically carbon-based so they will transmit to the detector similar electron outputs due to the low contrast.[107] Staining with heavy metal elements is the main method to mitigate contrast issues. Positive stains chemically bond directly to the sample (making the sample material itself have more contrast) while negative stains (more common because of its relative ease of use), surround the outline of the sample, making the background around the sample have more contrast.[107] Common negative stains include uranyl acetate, ammonium molybdate, and other heavy metal solutions. When applying the stain to the sample, a common method is to add a droplet of stain solution to the sample, which is allowed to sit for several seconds before removing the excess. Several techniques to remove excess stain have been used, including wicking or dabbing off the solution droplet with a clean tissue, rinsing with droplets of water, or dunking in a bath of water before drying.[40] TEM was used in this thesis to visualize the image of the composite formed through the in-situ polymerization of PPy in CNC.

5.5. FOURIER TRANSFORM INFRARED SPECTROSCOPY

Infrared (IR) spectroscopy is a vibrational spectroscopy technique that provides information about characteristic molecular vibrations, from which structural information about materials can be interpreted. The IR spectral range is between the visible and microwave regions and stretches from 14000 cm^{-1} to 10 cm^{-1}. It is divided into three regions: the near-infrared (14000 to 4000 cm^{-1}), mid-infrared (4000 to 400 cm^{-1}) and far-infrared (about 400 to 10 cm^{-1}). The most frequently used region for chemical analysis is the mid-infrared region since molecules can absorb radiation in this region to induce the vibrational excitation of functional groups.[108] When IR radiation is passed through a sample, the frequencies equivalent to the active vibrational modes of the molecules of the sample are to some extent absorbed, while other frequencies are transmitted through the sample without being absorbed by the sample. Radiation of various wavelengths can be absorbed depending on the chemical composition of the sample. The output is an IR spectrum in which the intensity of IR radiation absorbed or transmitted is plotted on the y-axis against the wavenumber of the radiation on the x-axis. The wavenumbers (reciprocal of wavelength in cm) are normally used to denote different wavelengths of radiation.

The prevalent form of IR is the Fourier Transform Infrared Spectroscopy (FT-IR) because of its good signal-to-noise ratio, maximum use of radiation, and high accuracy and stability.[109] In FT-IR, infrared spectra are collected as a time-domain spectrum of the sampled signal using a Michelson interferometer. Thereafter, a mathematical transformation called the Fourier transform is applied to the time-domain spectrum to obtain the frequency domain spectrum. This spectrum is then compared to a reference spectrum measured without the sample (background) to obtain the absorbance or transmittance spectrum. FT-IR spectroscopy can be used with different sampling techniques and modes of operation. Amongst the different techniques, the Attenuated Total Reflectance (ATR) is the most popular sampling technique in FT-IR spectroscopy. In this technique, the sample without any treatment is placed in contact with the internal reflection element also called ATR crystal, and IR radiation from the source is directed through the crystal to its surface that is in contact with the sample at a certain angle so that the light is reflected. The refractive index of the crystal must be higher than that of the sample for the total reflection to occur. Therefore, high refractive index materials are chosen for the ATR crystal. Some of the most used crystals are diamond, zinc selenide, and

germanium. FTIR-ATR spectroscopy was used in this thesis to analyze the structure of the hydrogel and confirm the incorporation of PPy in the hydrogel.

5.6. UV-VISIBLE SPECTROSCOPY

Ultraviolet-visible (UV-Vis) spectroscopy is an analytical technique that exploits light in the ultraviolet, visible, and near-infrared range of the electromagnetic spectrum. Beer-Lambert law (**Equation 3**) establishes a linear relationship between absorbance (A), the molar extinction coefficient (ε) and concentration of absorbing species (c) in the solution, and the path length (l). Hence, UV/Vis spectroscopy can be used to quantitatively ascertain the concentration of the analyte in a solution.[110]

$$A = \in lc \qquad \textbf{Equation 3}$$

In a UV-Vis test, samples are placed in a cuvette, which is rectangular-shaped with an internal width of 1 cm (i.e., path length l). A light beam is passed through the cuvette and part of the light is absorbed by the sample being analyzed while the rest proceeds to the detector. The wavelength of the light reaching the detector is measured. The measured wavelength provides important information about the chemical structure and concentration (intensity of the measured signal) of the sample measured. Hence, both quantitative and qualitative information can be gathered. The absorption of incident energy promotes electrons to excited states. For this transfer to occur, photon energy must match the energy needed by the electron to be promoted to the next higher energy state. In addition, the shift in wavelengths of absorption peaks of a sample in the UV-Vis absorption spectrum can be correlated to band gap change (due to movement of electrons from the valence band to the conduction band) of electrically conducting polymers.

The optical properties of a conducting polymer are important to the development of an understanding of the basic electronic structure of the material. The π-conjugation in the polymers is shown by their color and their electronic spectra; thus UV-Vis spectroscopy is a powerful technique for characterization of the electronic processes that occur in the polymer in the undoped and doped states, as well as during doping.[111] The changes of the optical spectra associated with doping are significant, and these spectral changes have played a key role in understanding the mechanism of doping and the nature of the charge-storage species in the polymer chain.[112] UV-Vis spectroscopy was used in this thesis to analyze the electronic state of PPy in the hydrogel ink.

5.7. TWO-POINT PROBE RESISTANCE

The resistivity of a sample can be measured with either the four-point probe or the two-point probe methods. The multimeter is an instrument that is commonly used for two-point probe measurements. In the two-point probe configuration, two identical electrodes serve as both current and voltage sensing probes.[113] A small amount of voltage is provided to the resistor via the contact probes of the multimeter, and the current flowing across the two contact points is recorded, thereby giving the resistance value following Ohm's law. The two-point probe measurement is the most common method used to determine the resistance of a material.[114] However, one inherent flaw in this method is that the same two contact probes used for providing the test voltage are also used for recording the current flowing due to the supplied voltage. Hence, the internal resistance of the probes gets added to the actual displayed value, thus, giving inaccurate results.[115] The four-point probe provides more reliable results because it has different probes for the current path and the voltage. Also, the two-point probe is not a perfect method for resistance measurements of ionic or polarizable systems such as electrically conducting polymers. Notwithstanding, the two-point probe method was used in this thesis to monitor whether the hydrogel inks showed conducting properties or not.

5.8. CYCLIC VOLTAMMETRY

Cyclic voltammetry (CV) is a type of potentiodynamic electrochemical technique commonly applied to study the mechanism of redox reactions of electroactive materials such as conducting polymer hydrogels.[85] It is usually performed in a 3-electrode electrochemical cell where the potential is cycled with a pre-determined scan rate in a certain potential range. As shown in **Figure 13**, the potential is scanned from E_1 to E_2 and after the potential reaches a set value, it is then ramped in the opposite direction back to the initial potential (E_1) or a third potential (E_3).[116]

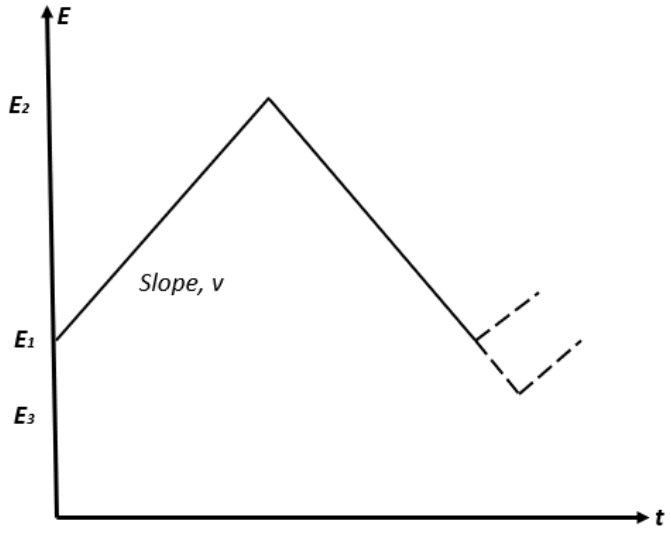

Figure 13. Potential-time profile in cyclic voltammetry. Image is adapted from "Potential Sweep Techniques and Cyclic Voltammetry," by Pletcher, D. *et al*., 1993, *Instrumental Methods in Electrochemistry*, Ellis Horwood Limited, Southampton, p. 179 (Copyright: Ellis Horwood Limited).

The potential is measured between the reference electrode and working electrode while the current produced in the process is controlled between the working electrode and the counter electrode. The plot of the current against the applied potential results in a cyclic voltammogram. The shape and positions of the voltammograms provide a key understanding of the properties of polymer structure such as the reversibility of the redox couple, and electron transfer kinetics. For reversible systems, the current is limited by diffusional mass transport, and the peak potentials (E_p) and peak separation (ΔE_p) do not depend on the scan rate. For irreversible systems, ΔE_p increases, and E_p shifts to more extreme potentials with increasing scan rate (more positive for oxidation, negative for reduction).[117] As shown by the Randles-Sevcik equation (**Equation 4**), there is a linear relationship between the peak current and the square root of the scan rate for electrochemically reversible electron transfer processes involving freely diffusing redox species.[118]

$$i_p = 0.446nFAC^0\left(\frac{nF\upsilon D_o}{RT}\right)^{1/2} \qquad \textbf{Equation 4}$$

Where i_p (A) is the peak current, D_0 (cm^2 s^{-1}) is the diffusion coefficient of the oxidized analyte, A (cm^2) is the electrode surface area, n is the number of electrons transferred in the redox event, C^0 (mol cm^{-3}) is the bulk concentration of the analyte, and v (V/s) is the potential scan rate. Cyclic voltammetry is commonly used to analyze the electroactivity, charge storage capacity,

and electrochemical stability of conducting polymer hydrogels.[119–121] CV was used in this thesis to assess the stability and electroactivity of the hydrogel after continuous potential cycling.

5.9. ELECTROCHEMICAL IMPEDANCE SPECTROSCOPY

Impedance is the opposition by an electrical system to the flow of electric current and carries units of Ohms, Ω.[122] Impedance differs from resistance because resistance is observed in DC circuits, and it obeys Ohm's law. Resistance is essentially impedance with zero phase angle since the current is not alternating.[122] In electrochemical impedance spectroscopy (EIS) experiments, a small amplitude sinusoidal excitation potential (E_{ac}) is superimposed on a fixed DC potential. At a set frequency, a current will flow through the electrochemical cell, and it is recorded by the potentiostat. The current is then converted by software into an impedance value with a real and imaginary component. This process is repeated across a frequency range where different values are deduced for the real and imaginary components of the overall impedance.[122]

EIS can reveal details regarding the conduction mechanism in a complex system such as a hydrogel and it has been used to study the cellular responses in bulk artificial and biological tissues.[123,124] Impedance can be expressed in terms of a magnitude, Z_0, and a phase shift, ϕ as shown in **Equation 5** below:

$$Z(\omega) = E/I = Z_0 \exp(j\phi) = Z_0(\cos\phi + j\sin\phi) \qquad \textbf{Equation 5}$$

Where $Z(\omega)$ is the complex impedance and consists of a real and an imaginary part, ϕ is the phase shift between the applied signal and resulting response. A phase shift of 0° corresponds to a pure resistor, 45° corresponds to a Warburg impedance due to diffusion limitation (**Figure 14**), and 90° corresponds to a capacitor. The impedance of a system is commonly presented as the Nyquist plot and Bode plot.[122]

The Nyquist plot or Complex-Impedance Plane representation (**Figure 14a**) is a plot in which the data from each frequency point is plotted by the imaginary part *(-Z")* on the y-axis and the real part (*Z'*) on the x-axis. The high-frequency intercept on *Z'* represents the ohmic resistance of the electrolyte (R_s). The low-frequency intercept gives the characteristic impedance of the system. Also, features such as the semicircle or a 45˚ low-frequency line give possible insight into the governing kinetic in the system.[122]

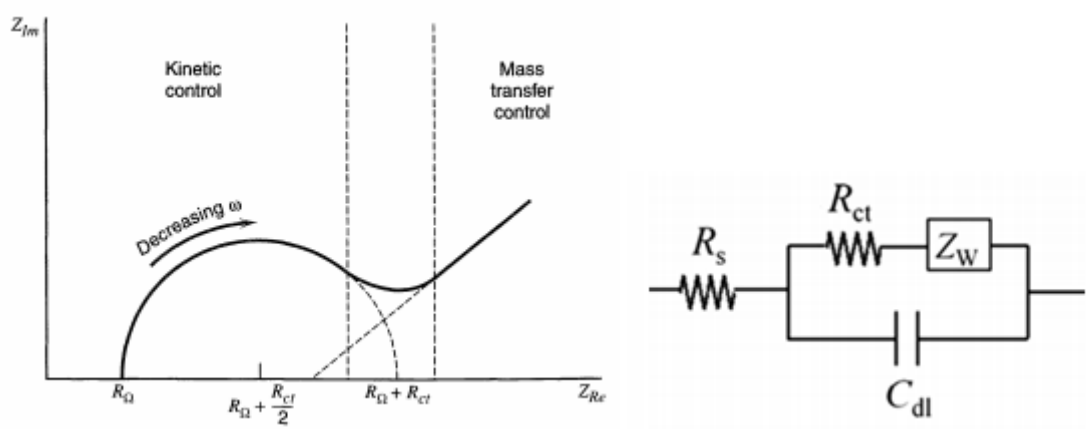

(a) **(b)**

Figure 14. (a) A typical shape of Nyquist plot from EIS and (b) equivalent electrical circuit. Image is adapted from "Electrochemical Impedance Spectroscopy," by Bard, A., and Faulkner, L. R., 2000, *Electrochemical Methods – Fundamentals and Applications, 2nd ed*, John Wiley & Sons, Inc, New York, p. 386 (Copyright: John Wiley & Sons, Inc).

In the Bode plot, the impedance magnitude and phase angle are plotted against frequency. The impedance magnitude is given by **Equation 6.**[125]

$$|Z| = \sqrt{(Z')^2 + (-Z'')^2} \qquad \textbf{Equation 6}$$

Interpretation of EIS data has traditionally relied on models containing equivalent electrical circuit elements (**Figure 14b**). The equivalent electrical circuit shown in **Figure 14b** is known as the Randle's circuit and it models a system in which a faradaic process occurs.[116,122] The Randle's circuit consists of the resistance of the electrolyte solution, R_s, charge transfer resistance, R_{ct}, Warburg element, Z_w, and the double layer charging at the electrode surface C_{dl}. The Z_w accounts for the diffusion of the ions in solution in an electrochemical reaction.[122] EIS was used in this thesis to assess the electroactivity and electroconductivity of the hydrogel after the incorporation of PPy.

6. HYPOTHESIS AND AIM OF THE STUDY

Although several materials have been explored for tissue engineering, many of them are not biocompatible. For example, the use of metal nanostructures and carbon-based materials (e.g. carbon nanotubes) is limited by their long-term cytotoxicity. Furthermore, current studies involving the use of electrically conducting polymers and biopolymers to fabricate hydrogels rarely assess the printability of the hydrogel inks. This study is based on the hypothesis that

CNC and PPy have excellent properties which make them suitable as starting materials for the synthesis of electroconductive hydrogel inks for 3D printing. CNC has excellent mechanical and rheological properties which makes it suitable as a reinforcing nanofiller in hydrogel inks. PPy which is a biocompatible polymer with excellent intrinsic electrical conductivity could provide the relevant electrical conductivity needed for the regeneration of electrically excitable tissues. Consequently, this work is aimed at:

- ✓ Developing a suitable formulation of CNC/PPy composite that is colloidally stable and without aggregation of the nanoparticles.
- ✓ Using the composite as a starting material to fabricate an electroconductive hydrogel with promising properties for tissue engineering.

7. EXPERIMENTAL

7.1. CHEMICALS AND MATERIALS

Pyrrole (Py, Sigma-Aldrich, ≥ 98.0%) was distilled under vacuum before use and stored tightly sealed in the dark at below 0 °C. Potassium chloride (KCl, ≥ 98.0%, Merck), Ammonium persulfate (APS, $(NH_4)_2S_2O_8$, ≥ 98.0%, Sigma-Aldrich), iron (III) chloride hexahydrate ($FeCl_3 \cdot 6H_2O$, ≥ 98.0%, Sigma-Aldrich) sodium hydroxide (NaOH, ≥ 98.0%, VWR chemicals BDH), sulphuric acid (H_2SO_4, ≥ 98.0%, Sigma-Aldrich), methacrylic anhydride (MA, ≥ 94.0%, Sigma-Aldrich), gelatin methacryloyl (GelMA, Allevi), lithium phenyl-2,4,6-trimethylbenzoylphosphinate (LAP, Sigma-Aldrich), cellulose dialysis tubing (12-14 kDa MWCO, Sigma-Aldrich), regenerated cellulose dialysis tubing (3.5 kDa MWCO, Spectra/Por), Whatman ashless filter paper (< 2 μm, Sigma-Aldrich), analytical grade microcrystalline cellulose (MCC, Sigma-Aldrich), and polyvinylpyrrolidone (PVP, average MW= 10,000, Sigma-Aldrich) were used as received. Ultra-pure MilliQ+ water (TOC ≤ 5 ppb, conductivity ≤ 0.054 μS/cm) and deionized water (ELGA Purelab Ultra; resistivity ~ 16.5 MΩcm) were used for sample preparation while 0.3 μm Al_2O_3 powder was used for polishing of the electrode. Galactoglucomannan (GGM) was provided by the Tree and Paper chemistry group at the Laboratory of Natural Materials Technology, Åbo Akademi University.

7.2. METHODS AND INSTRUMENTATION

7.2.1. CV AND EIS

Electrochemical studies consisting of cyclic voltammetry (CV) and electrochemical impedance spectroscopy (EIS) were done in a conventional three-electrode one-compartment cell connected to Autolab PGSTAT30 potentiostat, Nova 2.1.4 software. To prepare the working electrode, an aqueous slurry of alumina powder (Al_2O_3) on a damp smooth polishing cloth was used for manually polishing the platinum (Pt) electrode (Ø = 3 mm). Adherent alumina powder was removed from the Pt electrode surface by rinsing with deionized water before polishing on a clean cloth without alumina. The Pt electrode was then sonicated in deionized water and dried in the air.

Before each CV and EIS measurement, the aqueous electrolyte solution (0.5 M KCl) was deaerated for 15 min with N_2 and all the measurements were performed in an N_2 atmosphere.

In the CV experiments, the Pt electrode potential was monitored against an Ag/AgCl/KCl (3M) reference electrode, and a glassy carbon rod formed the counter electrode. CV measurements were performed using five (5) potential cycles from -0.4 V to 0.4 V at scan rates of 10 mV/s and 20 mV/s. The measurements were repeated five times for each scan rate with five (5) potential cycles for each measurement.

Immediately after the CV measurements, EIS measurements were performed at a frequency range of 0.1 Hz to 100 kHz. All measurements were done with an AC voltage amplitude (E_{ac}) of 10 mV and at DC potential (E_{dc}) of 0 V. The impedance spectra obtained were fitted to an equivalent electrical circuit using the NOVA Autolab impedance analysis software which exploits a nonlinear least square regression to fit the data using the Levenberg–Marquardt algorithm. The Bode plots (log of frequency vs impedance magnitude, $|Z|$) and Nyquist plots (Z' vs -Z") were plotted with data extracted directly from the software. The EIS measurements were repeated 10 times.

7.2.2. ZETA-POTENTIAL AND DYNAMIC LIGHT SCATTERING

Zeta-potential (ZP) and dynamic light scattering (DLS) measurements were done using a Malvern zeta sizer Nano series (zeta sizer software 7.11). The ZP of the samples suspended in deionized water (0.01 wt %) was measured to determine the stability and surface charge of the samples. The samples were sonicated in an ultrasonic bath for 30 min before measurements.

For each sample, after equilibration for 2 min at 25 ℃, five measurements were done with 10 to 100 runs per measurement. Although electrophoretic mobility was recorded, it is directly proportional to the particle surface charge without assumptions of particle shape/size/charge density.[126] The electrophoretic mobility was converted to zeta-potential with the Smoluchowski approximation in Henry's equation (**Equation 1**).

DLS was used to measure the apparent diameter of the samples (0.01 wt %) at 25 ℃. The term "apparent diameter" is used because, in DLS measurements, the particles are recognized as spherical, and the hydrodynamic diameter is measured but CNCs which served as the template for all the samples in this thesis are rod-shaped. However, for non-spherical particles, the hydrodynamic diameter is the diameter of an imaginary sphere that produces the same translational coefficient as the real particle of arbitrary shape hence the hydrodynamic diameter for CNC is an approximate size measurement and it is accepted as a reliable metric for comparison purposes.[126,127] Also, diluted solutions are needed for DLS measurements because the Stokes-Einstein equation that relates the translational coefficient to the hydrodynamic diameter is applicable only for dilute solutions.[128] For each sample, after equilibration for 2 min at 25 ℃, five measurements were done with 10 to 100 runs per measurement at a 173° scattering angle. This optimum angle was selected because the scattering power of nano-sized particles at a large scattering angle (173°) contains enough information for a general interpretation procedure.[128] The Mean particle size is reported as the average hydrodynamic diameter (D) based on **Equation 2** and determined by the instrument's software.

7.2.3. UV–VIS ANALYSIS

For the CNC/PVP/PPy/GelMA hydrogel inks, the UV-visible spectra were measured using 100 µl of the sample diluted with 3 ml of deionized water, while the background spectrum was recorded with 100 µl of CNC/PVP/GelMA diluted with 3 ml of deionized water. Pristine PPy spectrum was recorded with 100 µl of dispersed PPy diluted with 3 ml of deionized water.

The UV-visible spectrum of the CNC/PPy/GGMMA/LAP hydrogel ink was recorded using 20 µl of the sample diluted with 3 ml of deionized water. The background spectrum was recorded with 20 µl of CNC/GGMMA/LAP diluted with 3 ml of deionized water. The spectrum for pristine PPy was recorded with 20 µl of dispersed PPy diluted with 3 ml of deionized water. The background for the pristine PPy was recorded with 3 ml of deionized water. The spectra

were recorded with a Perkin-Elmer Lambda 25 spectrophotometer between 300 and 1100 nm at a scan rate of 480 nm min^{-1} with a 1 cm path length quartz cuvette.

7.2.4. FTIR-ATR ANALYSIS

The FTIR spectra were obtained with a Bruker IFS 66/S FTIR instrument equipped with a DTGS detector. The ATR set-up consists of Harrick's VideoMVP single reflection diamond ATR accessory with a horizontal sampling area of 500 µm in diameter, and a built-in pressure applicator. This technique was used for the structural analysis of the hydrogel to confirm the incorporation of PPy. The prepared dry samples (freeze-dried hydrogel and pristine PPy) were tightly pressed against the diamond crystal during the measurements. The angle of incidence of the infrared beam was 45°. For each measurement, 32 interferograms were co-added and the FTIR spectra were recorded in % transmittance mode in the wavelength range of 5000 to 500 cm^{-1} with a resolution of 4 cm^{-1}.

Before the analysis, the hydrogel was frozen in an ultra-low-temperature freezer at -40 ℃ for about two hours. After being completely frozen, the sample was transferred to a freeze-dryer (Alpha 1-4 LD Plus) and lyophilized under vacuum (0.067 mbar) at room temperature with an ice condenser operating at – 52 ℃. The hydrogel was kept in the freeze-dryer for 24 h to sublimate the solvent directly from the solid phase to the gaseous phase.

7.2.5. TEM/SEM

The transmission electron microscopy (TEM) was done using the JEM-1400 Plus TEM microscope, JEOL Ltd., Japan. A drop of the diluted sample suspension with a concentration of 0.01 wt % was deposited on the copper grids (200 mesh, TED PELLA INC. USA) coated with thin carbon film which was used as the substrate. The grids were then incubated at room temperature for 3 min and the excess liquid was eliminated by blotting with filter paper before loading in the microscope. Before the deposition of the sample, the grids were glow-discharged for 25 sec to increase their hydrophilicity. Also, before the analysis of pristine CNC, the sample was incubated in 3 µl of 0.5 wt% uranyl acetate solution for 1 minute to produce a negative stain contrast but the composite with polypyrrole did not require staining. The analysis was carried out with an accelerating voltage of 80 kV.

The scanning electron microscopy (SEM) measurements were done using the LEO Gemini 1530 SEM microscope (Oberkochen, Germany) equipped with a Thermo Scientific UltraDry

Silicon Drift Detector (Thermo Scientific Inc., Madison, Wisconsin, U.S.A). For the SEM analysis, the freeze-dried hydrogel was attached to an aluminum plate with carbon tape and further sputtered with carbon to increase the electrical conductivity and prevent charging. After analysis of the surface morphology, the hydrogel was divided using liquid nitrogen, then the cross-sectional morphology was analyzed.

7.2.6. TWO- POINT PROBE RESISTANCE MEASUREMENT

The resistance of the composites and hydrogel inks was monitored using a UNI-T UT 58B general digital multimeter with an upper resistance limit of 200 MΩ. 100 µl of the samples (Ø = 1 cm) were pipetted on a glass slide and allowed to dry in air, to form a thin film. The probes of the multimeter were placed on the ends of the thin film and the instrument was checked for the response. If the sample is conductive, the instrument shows the resistance in ohms but if the sample is not conductive, there is no response on the multimeter.

7.3. PREPARATION OF CELLULOSE NANOCRYSTALS

The CNCs were extracted from microcrystalline cellulose (MCC) by acid hydrolysis according to previously described methods[37,42] with minor adjustments. In this project, 200 ml of sulfuric acid (64 wt%) was allowed to heat up in an oil bath for 15 min before adding 14 g of MCC. The hydrolysis of MCC was done under mechanical stirring for 90 min at 45 °C and the reaction was stopped by adding the sample into 2 l of cold distilled water. The diluted suspension was centrifuged with Milli-Q water four times at 4000 rpm for 20 min. This was done to remove the sulfuric acid from the suspension. The CNC precipitate was then rinsed and dialyzed using cellulose dialysis tubing (12-14 kDa MWCO) in DI water. The dialysis was done for 9 days with the DI water being changed three times daily until constant conductivity and neutral pH in the effluent were achieved. Finally, the suspension was dispersed with an AH-basic high-pressure homogenizer by one pass at a pressure of 600 bar and two passes of 1000 bar to obtain a homogeneous suspension. The final suspension was ca. 2.15 wt% CNC in water and it was stored at 4 °C for further analyses.

7.4. PREPARATION OF GGMMA

Galactoglucomannan methacrylate (GGMMA) was synthesized by reacting galactoglucomannan (GGM) with methacrylic anhydride based on the method reported in the literature with slight adjustments.[67] Briefly, 2 g of GGM was dissolved in 100 ml of deionized water at 50 °C then 4 ml of methacrylic anhydride was added to synthesize GGMMA. The

reaction continued for 3 h with pH maintained at 8.0 by the addition of 6.0 M NaOH. The GGMMA was purified by dialysis against Milli-Q water with regenerated cellulose dialysis tubing (3.5 kDa MWCO). The GGMMA was obtained by lyophilization and stored as dry and protected from light before further use.

7.5. PREPARATION OF HYDROGEL INKS

As stated earlier in the literature review, the biomaterials for the formulation of 3D printable electroconductive hydrogels for tissue engineering must possess certain physical and chemical properties. In addition to enhanced electroconductivity, the materials need to be integrated into a stable colloidal dispersion. To achieve these goals, different methods were explored to synthesize the composite biomaterials which constitute the hydrogel inks. A common procedure in all the methods is the in-situ chemical polymerization of PPy using CNC as the matrix.

7.5.1. METHOD 1: PREPARATION OF GelMA HYDROGEL WITH CNC/PVP/PPy COMPOSITE

A composite of cellulose nanocrystals, polyvinylpyrrolidone, and polypyrrole (CNC/PVP/PPy) was synthesized as a starting material before mixing with GelMA to form the hydrogel ink. The PVP was used because it is an amphiphilic surfactant that can form a hydrophobic layer on the surface of CNC and promote the uniform coating of PPy.[129] Wu et al. reported an increase in conductivity when PVP was used in the in-situ polymerization of PPy in CNC.[95] Hence, it is expected that the use of PVP would provide enhanced electroconductivity for the hydrogel.

The CNC/PVP/PPy was synthesized according to the method described by Wu et al.[95] with some modifications. In this project, 0.2 wt% CNC solution was mixed with PVP at a PVP/CNC mass ratio of 10:100. The mixture was stirred vigorously overnight to ensure homogeneity. Then 15 ml of the CNC/PVP mixture was transferred to a double-jacketed reaction vessel kept in an ice water bath at around 0 ^{o}C and 5 ml of 0.45 M of $FeCl_3 \cdot 6H_2O$ was added dropwise to the suspension and vigorously stirred. After one hour, 106.5 µl of pyrrole monomer (Py) dissolved in 5 ml water was added slowly for 30 min and the suspension was left to mix under mild stirring for 16 h. The reaction was ended by repeatedly washing the dispersion with deionized (DI) water on a Whatman ashless filter paper, using a Büchner funnel to remove excess oxidants and unreacted monomers. After washing, the CNC/PPy slurry was dispersed

in DI water with probe sonication to form a stable suspension. The dispersed solution was then mixed with GelMA to form the hydrogel ink.

7.5.2. METHOD 2: PREPARATION OF GelMA HYDROGEL VIA IN-SITU POLYMERIZATION OF POLYPYRROLE IN CNC/PVP/GelMA

Another method was explored to fabricate an electroconductive hydrogel according to a previously described method with some modifications.[25] 0.3 g of GelMA was added to 15 ml of CNC/PVP solution and kept in warm water of ca. 37 ºC to dissolve the GelMA. The CNC/PVP solution was prepared using the same procedure described in method 1. After the GelMA was completely dissolved, the mixture was stirred vigorously for 30 min. This was followed by the dropwise addition of pyrrole to the mixture and the stirring continued for 2 h at room temperature. Afterward, APS was added to initiate the polymerization. The compositions of the samples studied are shown in **Table 1.**

Table 1. The composition of the CNC/PVP/GelMA/PPy hydrogel inks

Samples	CNC (wt%)	Py (M)	APS/Py (Molar ratio)	GelMA (wt%)
GelMA-H-1	0.2	0.05	0.5	2
GelMA-H-2	0.2	0.05	1	2
GelMA-H-3	0.2	0.1	1	2
GelMA-H-4	0.2	0.1	2	2
GelMA-H-5	0.2	0.2	1	2

The reaction was left for 24 h under mild stirring after which the black solution (indicating the formation of polypyrrole) was dialyzed in DI water using cellulose membrane tubing with a molecular weight cut-off of 14 kDa. The dialysis was done to remove excess oxidants and unreacted monomers and the water in the beaker was changed three times daily. The dialysis was done for about 5 days until a constant conductivity of the effluent was achieved.

7.5.3. METHOD 3: PREPARATION OF GGMMA HYDROGEL FROM CNC/POLYPYRROLE COMPOSITE

The CNC/polypyrrole (CNC/PPy) nanocomposite was synthesized via an in-situ chemical polymerization according to previously described methods with some modifications.[93,95] Pyrrole (Py) monomer was added to 15 ml of CNC (**Table 2**) in a double-jacketed reaction vessel before adding APS as an oxidant to initiate the polymerization. The CNC and Py

monomer were initially mixed in the reaction vessel via rigorous stirring for 1 h with water circulating the vessel to maintain a temperature below the room temperature. After an hour, APS dissolved in 5 ml of DI water was added dropwise for 30 min to initiate the polymerization. The samples and their formulations are shown in **Table 2.**

Table 2. The composition of the CNC/PPy composites mixed with GGMMA

Samples	CNC (wt%)	Py (M)	APS/Py (Molar ratio)
CNC/PPy-1	0.2	0.2	2
CNC/PPy-2	0.2	0.1	1.5
CNC/PPy-3	1	0.2	2
CNC/PPy-4	1	0.1	1.5
CNC/PPy-5	2	0.2	2
CNC/PPy-6	2	0.1	1.5

The polymerization continued under mild stirring for 6 h and the reaction was quenched by repeatedly washing the dispersion with DI water on a filter paper, using a Büchner funnel to remove excess oxidants and monomers. After washing, the CNC/PPy slurry was dispersed in DI water via probe sonication for 1 h each at an amplitude of 38 μm to form a stable suspension. The dispersed solution was then mixed with 6 wt% GGMMA to form the hydrogel ink.

8. RESULTS AND DISCUSSION

This project aimed at the fabrication of an electroconductive hydrogel in 3D printing formulation for use in tissue engineering applications. To achieve this goal, biocompatible materials were used in a series of hydrogel ink preparation methods. This section details the significant improvements in the physical and chemical properties of the hydrogel inks from the first method (method 1) to the last method (method 3).

8.1. METHOD 1: PREPARATION OF GelMA HYDROGEL INK FROM CNC/PVP/PPy COMPOSITE

Method 1 was adopted to prepare a composite of CNC, PVP, and PPy (**Figure 15a**) which was mixed with GelMA to form the hydrogel ink. The GelMA (6.4 wt%) was mixed with 1 % of CNC/PVP/PPy and 0.5 wt% LAP to form the hydrogel ink. The ink was cast into a mold and crosslinked with exposure to UV irradiation at 365 nm for 9 min to form a hydrogel (**Figure 15b**).

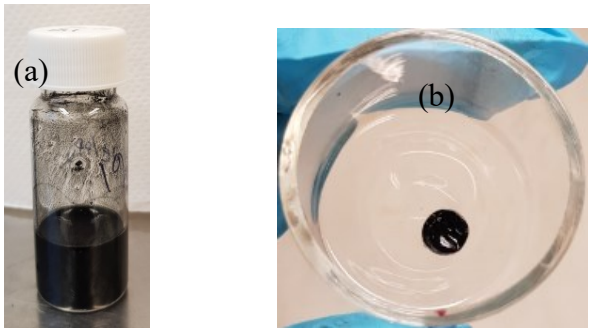

Figure 15. (a) CNC/PVP/PPy showing visible particles on the wall of the sample bottle; (b) CNC/PVP/PPy/GelMA hydrogel formed by casting.

PVP was used in this study because it is an amphiphilic surfactant that forms a hydrophobic layer on the surface of CNC and promotes the uniform coating of PPy.[129] Wu et al. reported an increase in conductivity when PVP was used in the in-situ polymerization of PPy in CNC.[95] Hence, it is expected that the use of PVP would provide enhanced electroconductivity for the hydrogel.

8.1.1. TEM ANALYSIS OF THE CNC/PVP/PPy COMPOSITES

Before mixing CNC/PVP/PPy with GelMA to form the hydrogel, the level of CNC surface modification with PVP and its effect on the growth of PPy were characterized with TEM and the results are shown in **Figure 16**. A noticeable size expansion of CNC/PVP/PPy particles was observed compared to pristine CNC without PVP. The TEM image confirms the successful polymerization of PPy to form a core-shell structure with the CNC as the core.

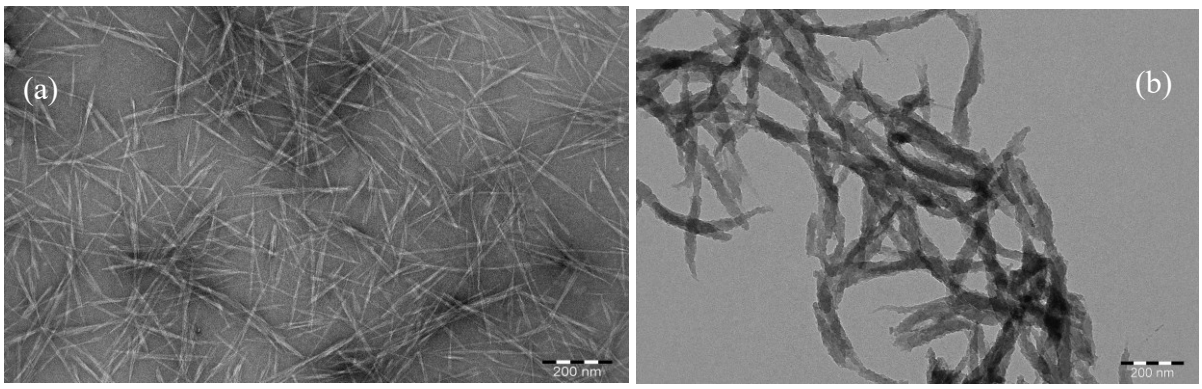

Figure 16. TEM images for (a) pristine CNC; (b) CNC/PVP/PPy.

8.1.2. SURFACE CHARGE AND PARTICLE SIZE MEASUREMENTS

Due to the negatively charged sulfate half-ester groups on the surface of CNC (i.e., OSO_3^-), it had a negative zeta-potential (ZP) of -67.0 ± 4.0 mV (n = 5), and it was very stable in an aqueous solution. After polymerization, the positively charged PPy neutralized the surface negative charges on CNC. The ZP increased to -6.0 ± 0.5 mV (n = 5) which signifies a homogeneous coating of PPy on CNC. Furthermore, the zeta-average size of the pristine CNC measured with DLS was 85 ± 6 d. nm (n = 5) while the zeta-average size of the composite (CNC/PVP/PPy) was 4846 ± 600 d. nm (n = 5). The remarkable difference in the zeta-average sizes can be attributed to the coating of the CNC/PVP by PPy which facilitated the aggregation of the particles due to reduction in electrostatic repulsion. The aggregation of the particles is visible as shown in the image in **Figure 15a**. The increase in particle size in the composite could also be visualized in the TEM image (**Figure 16b**) which shows a remarkable increase in size after the polymerization. Furthermore, the particles were not stable for a long period. The particles precipitated after about 5 h and this was due to the reduction of the number of free sulfate half-ester groups on the surface of CNC which provided colloidal stability to the composite. In agreement with the present results, previous studies have proven that stabilization of particles in solution by electrostatic repulsion arises from the particles' surface charge.[104,130] Hence, reduction of the surface charge affects the colloidal stability of the particles and causes aggregation. The results in this thesis are consistent with earlier studies which state that the ability of particles to resist aggregation and coagulation is indicated by the ZP values greater than +30 mV or less than -30 mV.[98,99]

Also, after the addition of GelMA to the CNC/PVP/PPy, further aggregation of the particles was observed. This can be attributed to further reduction of the electrostatic repulsion due to the interaction between the negatively charged sulfate half-ester groups on the surface of the CNC and the positively charged arginine.[131,132] Arginine has a high intrinsic pK_a value (13.8) which ensures that it is always protonated, even at pH values as high as 10.[133] Also, unlike other basic and acidic amino acids, arginine can remain charged even when buried in a hydrophobic micro-environment such as proteins, which is incompatible with the presence of a charged group.[133] As stated in the literature review, chemical modification of gelatin by MA does not affect the RGD motifs (Arginine-glycine-aspartate) because they do not contain groups that can react with MA,[71] which ensures the availability of the positively charged arginine for electrostatic interaction with CNC.

Furthermore, it is believed that there is a complexation between the Fe^{3+} from the oxidant and the OSO_3^- groups on CNC which further contributes to the reduction of the electrostatic repulsion and thus leads to aggregation of the particles. The strong relationship between Fe^{3+} and the dopant ion (PSS^-) during the polymerization of polypyrrole has been reported in a previous study.[94] Hence, to eliminate the possible electrostatic interaction between Fe^{3+} from the oxidant and the OSO_3^- of CNC, $FeCl_3 \cdot 6H_20$ was replaced by APS in the subsequent methods.

8.1.3. ELECTRICAL RESISTANCE OF THE CNC/PVP/PPy/GelMA HYDROGEL INK

Finally, the resistance of the hydrogel ink was checked with the two-point probe measurement. There was no response on the multimeter when the dry film of the hydrogel ink was tested. This was possibly due to the high number of insulators (CNC, PVP, and GelMA) in the hydrogel ink which broke the network of PPy and affected the conductivity.

Considering the results of the various characterization techniques, the hydrogel ink synthesized with this method was not suitable for high-quality 3D printing. The particle aggregation observed in the hydrogel ink was indicative of poor colloidal stability which could affect the resolution and precision of the tissue scaffold during 3D printing. Although the electroconductivity could be induced by increasing the Py monomer concentration and oxidant:monomer ratio, the poor colloidal stability of the hydrogel ink was still a major factor. Hence, the hydrogel ink was not worth further characterizations.

8.2. METHOD 2: PREPARATION OF GelMA HYDROGEL VIA IN-SITU POLYMERIZATION OF POLYPYRROLE IN CNC/PVP/GelMA

In method 2, an in-situ chemical polymerization of PPy in a mixture of CNC, PVP, and GelMA was done. This method was adopted to achieve a good network of PPy in the hydrogel ink. Different hydrogel inks were prepared, and their compositions are shown in **Table 1**.

8.2.1. SURFACE CHARGE AND PARTICLE SIZE MEASUREMENTS

As seen in **Figure 17**, the particles in the hydrogel ink prepared with method 2 were not stable, not homogenous, and they were very large.

Figure 17. CNC/PVP/GelMA/PPy hydrogel ink.

As stated in method 1, this is due to the reduction in the ability of CNC to stabilize the dispersion because of the decrease in the number of free OSO_3^- groups on the surface of CNC due to the polymerization of PPy. Also, the electrostatic interaction between the negatively charged sulfate half-ester groups of CNC and the amino acid (arginine) in gelatin contributes to the reduction in the electrostatic repulsion of the particles.[131–133] **Table 3** shows the significant difference in the ZP values of the hydrogel inks compared to pristine CNC. This further confirms the reduction in electrostatic repulsion in the hydrogel inks. These findings are consistent with previous studies that ZP values greater than +30 mV or less than -30 mV indicate the ability of particles to resist aggregation and coagulation.[98,99]

Table 3. The zeta-potential and zeta-average size of particles in the CNC/PVP/GelMA/PPy hydrogel inks prepared by method 2 and their comparison with pristine CNC

Samples	*Z*-potential (mV)[a]	*Z*-average size (d. nm)[a]
GelMA-H-1	2.26 ± 0.14	4782 ± 1400
GelMA-H-2	-0.99 ± 0.21	7828 ± 3700
GelMA-H-3	6.16 ± 0.25	3113 ± 180
GelMA-H-4	6.81 ± 0.45	1902 ± 260
GelMA-H-5	7.50 ± 0.22	6121 ± 500
Pristine CNC	-67.0 ± 4.0	85 ± 6

[a]Each value represents an average of 5 measurements, and the confidence intervals are the repeatability standard deviation.

A closer inspection of the data for the *Z*-average size in **Table 3** shows that there is a high disparity in the size measurement amongst the different samples despite very little difference in their composition. This can be attributed to the limitation in the DLS technique which was used to measure the sizes of the particles. DLS is unable to differentiate between particles with

slight differences in diameter or to precisely resolve polydisperse samples (see **Figure 17**).[103] This could skew the results in favor of the large particles and also affect the repeatability of measurements.

8.2.2. ELECTRICAL RESISTANCE OF THE CNC/PVP/GelMA/PPy HYDROGEL INK

The two-point probe method (multimeter) was used to monitor the effects of the Py monomer concentration and the oxidant:monomer ratio, on the resistance of dry hydrogel inks. In the first samples prepared, 0.05 M of Py was used and the resultant hydrogel ink was not conductive after testing with the multimeter. After the increase in the concentration of Py to 0.1 M (APS/Py ratio of 1 and 2) and 0.2 M (APS/Py ratio of 1), there was a decrease in resistance of dry hydrogel films, and this resulted in a response on the multimeter. These findings are consistent with the results of Liu et al.[134] who reported that the conductivity of polypyrrole-based cellulose composites correlates with the concentration of Py monomer.

8.2.3. ANALYSIS OF THE OXIDATION STATE OF PPy IN THE CNC/PVP/GelMA/PPy HYDROGEL INK

To gain a better insight into the state of PPy in the composite, UV-Vis spectra of the samples were recorded. UV-Vis spectroscopy is a valuable tool for analyzing changes in the electronic structure of electrically conducting polymers and to characterize the doping state in which they exist. The UV-Vis spectra of the CNC/PVP/GelMA/PPy hydrogel inks and pristine PPy are shown in **Figure 18**.

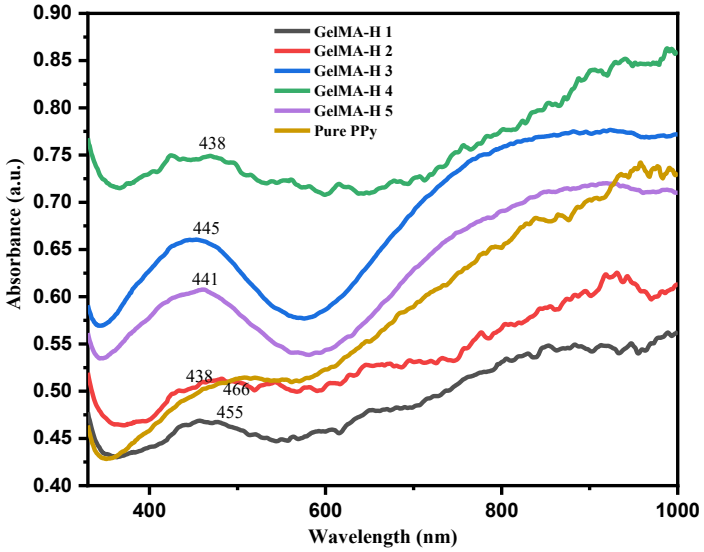

Figure 18. UV-Visible spectra of the CNC/PVP/GelMA/PPy hydrogel inks prepared with method 2.

The samples showed absorbance between 438 nm and 466 nm which is characteristic of the π-π* transition in PPy.[93,135] The broad absorption band from the visible region to the near-infrared region is characteristic of the bipolaronic metallic state of doped PPy.[136] These results confirmed that the PPy in the hydrogel inks was in its conducting form. Despite being in the conductive state, at the low concentration of Py (0.05 M) in GelMA-H 1 and GelMA-H 2, the repeating units of Py ring structures did not form a conductive network in the composite. These results provided important insights which helped in developing suitable parameters for the synthesis of the hydrogel inks in the next method.

Due to the large particle sizes and the instability of the dispersion, the hydrogel inks prepared with this method were not suitable for high-quality 3D printing. The particle aggregation and poor colloidal stability observed in the hydrogel ink could affect the resolution and precision of the tissue scaffold structures. Another limitation of this hydrogel ink was revealed by the work of Wang et al.[25] which showed that the in-situ polymerization of PPy in GelMA leads to the grafting of PPy on the double bond of MA. The absence of the double bond in the photoreactive moiety could limit its potential to be crosslinked using photoinitiators. Also, due to the electrostatic interaction between the charged arginine and the sulfate half-ester groups, GelMA was not considered for further formulation of the hydrogel ink, and the hydrogel ink formed with this method was not characterized any further.

8.3. METHOD 3: PREPARATION OF GGMMA HYDROGEL WITH CNC/PPy COMPOSITE

Based on the knowledge obtained from the previous methods, a third method was developed to prepare the hydrogel ink. The polymerization time was reduced to 6 h, as it has been reported as the ideal time required to obtain good conductivity from PPy as well as moderately low zeta potential.[95] A total of six samples with different formulations were prepared, as shown in **Table 2**. Also, PVP was excluded in the formulation of the hydrogel ink, as it was observed based on TEM images from the first method that PVP promoted the formation of a core-shell structure of CNC/PVP/PPy with a large particle size. PVP is also an insulator that could impede the conductivity of PPy in the hydrogel ink.

8.3.1. SURFACE CHARGE AND PARTICLE SIZE MEASUREMENTS

The CNC/PPy samples were left standing and undisturbed to confirm the stability and dispersibility of the nanocomposites. Samples CNC/PPy-1 and CNC/PPy-2 precipitated after 14 h, while samples CNC/PPy-3 to CNC/PPy-6 remained stable without precipitating (**Figure 19**). The poor colloidal stability and aggregation of particles in samples CNC/PPy-1 and CNC/PPy-2 could be due to the reduction in electrostatic repulsion because of the coating of the CNC by PPy which decreased the number of free sulfate half-ester groups on the surface of CNC.

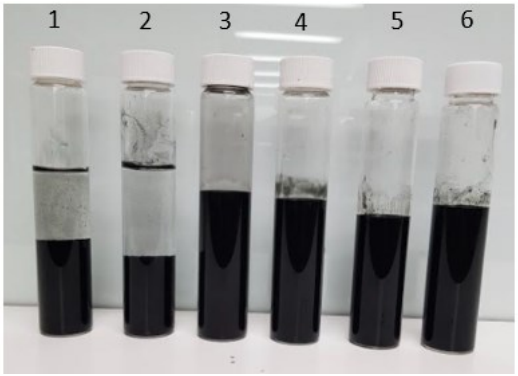

Figure 19. Samples prepared by method 3 left standing and undisturbed for 14 h after probe sonication.

The particles in samples CNC/PPy-3 to CNC/PPy-6 remained stable without aggregation nor precipitation because of the amount of free sulfate half-ester groups on their surface due to the higher concentration of CNC. These observations were further confirmed by the measured ZP of the samples (**Table 4**).

Table 4. The zeta-potential and zeta-average size of the CNC/PPy composites in comparison with pristine CNC

Samples	*Z*-potential (mV)[a]	*Z*-average size (d. nm)[a]
CNC/PPy-1	-11.60 ± 0.30	4407 ± 140
CNC/PPy-2	-22.9 ± 1.0	5937 ± 800
CNC/PPy-3	-31.9 ± 1.0	2865 ± 140
CNC/PPy-4	-37.9 ± 0.6	982 ± 19
CNC/PPy-5	-40.76 ± 0.38	1107 ± 8
CNC/PPy-6	-35.3 ± 1.4	1067 ± 22
Pristine CNC	-67.0 ± 4.0	85 ± 6

[a]Each value represents an average of 5 measurements, and the confidence intervals are the repeatability standard deviation.

For samples CNC/PPy-3 to CNC/PPy-6, the high negative ZP showed that there were still enough free sulfate half-ester groups on the surface of the composites to enable stability and prevent particle aggregation. However, samples CNC/PPy-1 and CNC/PPy-2 showed a less negative ZP which signifies an almost total coating of PPy on CNC. These findings are consistent with previous studies that ZP values greater than +30 mV or less than -30 mV indicate the ability of particles to resist aggregation and coagulation.[98,99]

Also, the DLS results showed an increase in hydrodynamic diameter of blended cellulose nanocrystals when compared to pristine CNC and this was indicative of the formation of a stable shell of PPy around the CNCs. The higher values obtained for samples CNC/PPy-1 and CNC/PPy-2 are due to the further aggregation of the particles. Due to the particle aggregation and precipitation in samples CNC/PPy-1 and CNC/PPy-2, they were not considered for further characterization.

8.3.2. ELECTRICAL RESISTANCE OF THE CNC/PPy/GGMMA HYDROGEL INK

To form the hydrogel inks, samples CNC/PPy-3 to CNC/PPy-6 were mixed with galactoglucomannan methacrylate (GGMMA) which does not have any surface charge. Therefore, GGMMA would not have any impact on the electrostatic repulsion of the nanoparticles in the hydrogel inks. For each sample, the resistance of the dry hydrogel inks (CNC/PPy/GGMMA) was tested with the two-point probe method. Amongst the samples, only

CNC/PPy-3 showed a response from the multimeter. It is believed that the combination of the high concentration of Py (0.2 M) and the low concentration of CNC (1 wt %) contributed to the low resistance in the hydrogel ink. Although 0.2 M Py was also used in CNC/PPy-5, the combined effect of high CNC amount (2 wt%) and the GGMMA which are both insulators could affect the network of PPy in the hydrogel ink and thus, affect the conductivity. Hence, hydrogel inks formed with CNC/PPy-3 were used for further investigation in this thesis.

8.3.3. ANALYSIS OF THE OXIDATION STATE OF PPy IN THE CNC/PPy-3/GGMMA HYDROGEL INK

To gain a better insight into the oxidation state of PPy, the UV-Vis spectrum of the hydrogel ink (1 wt% CNC/PPy-3 + 6 wt% GGMMA + 0.5 wt% LAP) was recorded (**Figure 20**).

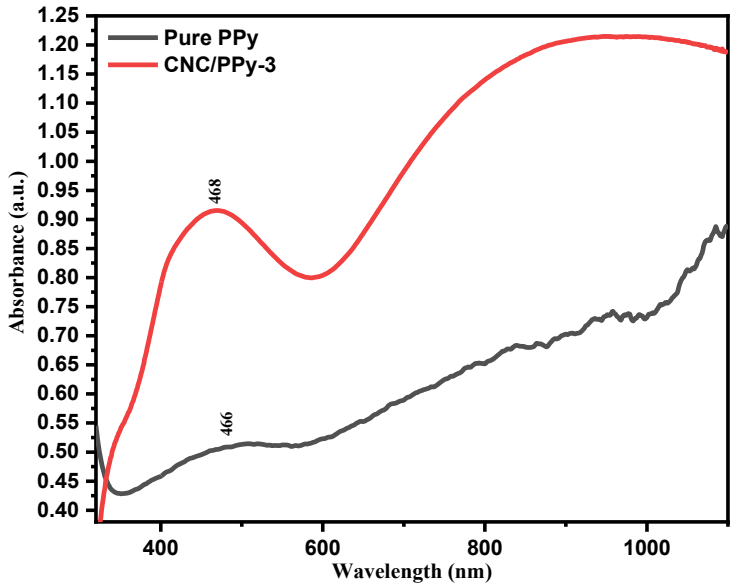

Figure 20. UV-Visible spectra of the hydrogel ink (1 wt% CNC/PPy-3 + 6 wt% GGMMA + 0.5 wt% LAP) prepared with method 3 and pristine PPy.

The samples showed absorbance at 468 nm and 466 nm which is characteristic of the π-π* transition in PPy.[93,135] The broad absorption band from the visible region to the near-infrared region is characteristic of the polaronic and bipolaronic metallic state of doped PPy.[136] These results confirmed that the PPy in the hydrogel inks was in its conducting form.

8.3.4. CNC/PPy/GGMMA HYDROGEL STRUCTURAL ANALYSIS

Fourier transform infrared (FTIR) spectroscopy was used to further verify the incorporation of PPy in the freeze-dried CNC/PPy-3/GGMMA hydrogel. The hydrogel ink (1 wt% CNC/PPy-3 + 6 wt% GGMMA + 0.5 wt% LAP) was crosslinked under UV irradiation at 365 nm and freeze-dried for the FTIR analysis. The spectra are shown in **Figure 21**. Most of the characteristic peaks for pristine PPy were observed in the CNC/PPy-3/GGMMA hydrogel including N-H stretching vibrations of Py rings at 3207 cm^{-1} and 3347 cm^{-1} and the fundamental C=C Py ring vibration at 1521 cm^{-1} and 1557 cm^{-1} (asymmetric ring stretching) for the pristine PPy and the CNC/PPy-3/GGMMA hydrogel, respectively. The peaks at 1281 cm^{-1} and 1302 cm^{-1} were attributed to C–N in-plane ring deformation (symmetric ring stretching) for the pristine PPy and the CNC/PPy-3/GGMMA hydrogel, respectively. The peak at 1015 cm^{-1} for the pristine PPy and 1029 cm^{-1} for the CNC/PPy-3/GGMMA hydrogel were due to the =C-H out of plane vibration and it indicates the polymerization of pyrrole. The peak at 1715 cm^{-1} seen in the CNC/PPy-3/GGMMA hydrogel represents the C=O stretching groups of MA. The peak at 1165 cm^{-1} seen in the CNC/PPy-3/GGMMA hydrogel was assigned to the C-O-C stretching vibrations in the CNC and GGM. The peak at 1632 cm^{-1} seen in the CNC/PPy-3/GGMMA hydrogel was assigned to the H-O-H deformation vibration of lattice water remaining in the CNC and GGM. The peaks obtained in this analysis were consistent with those available in the scientific literature[44,91,93,137–143] and the spectrum of the hydrogel was in good agreement with that of the pristine PPy, which indicates the incorporation of PPy in the CNC/PPy-3/GGMMA hydrogel.

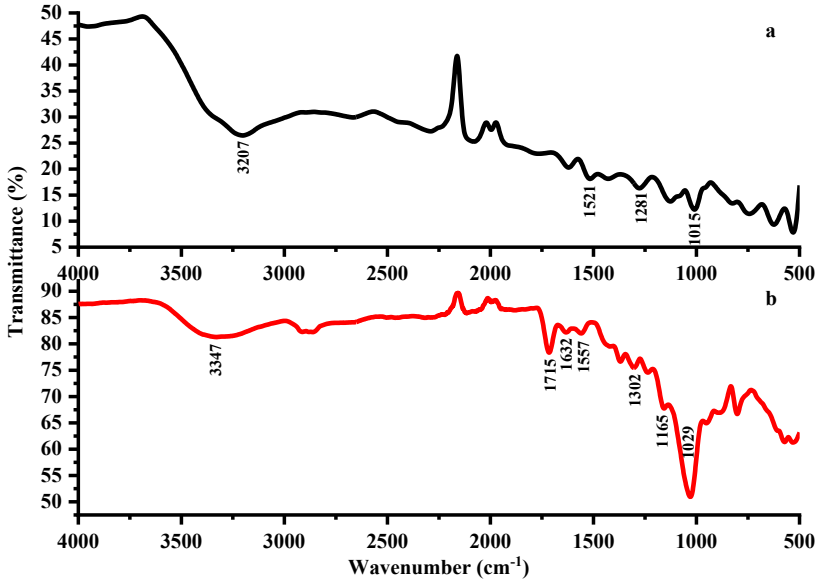

Figure 21. FT-IR spectra of (a) pristine PPy, and (b) CNC/PPy-3/GGMMA hydrogel.

Also, it was observed that the peaks of the CNC/PPy-3/GGMMA hydrogel shifted towards higher wavenumbers in comparison to that of pristine PPy. For instance, it can be seen in **Figure 21** that the C=C stretching vibration of Py rings which appeared at 1521 cm^{-1} for pristine PPy shifted to a higher wavenumber at 1557 cm^{-1} in the CNC/PPy-3/GGMMA hydrogel. Similarly, the absorption band at 1281 cm^{-1} in pristine PPy shifted to a higher wavenumber at 1302 cm^{-1} in the CNC/PPy-3/GGMMA hydrogel. Bober et al.[143] reported that the shift of this absorption band (from 1281 cm^{-1} to 1302 cm^{-1}) could be due to the hydrogen bonding interactions between the N-H groups in the Py rings and the lone pair of electrons on the oxygen atom of the -OH groups on the surface of GGM and CNC. On the other hand, the hydrogen atoms of the CNC and GGM -OH groups can interact with the lone pair of electrons on the Py nitrogens.[144] Another reason for the blue shift of this band could be due to the different degrees of doping of PPy which leads to lower conductivity of the composite (CNC/PPy-3/GGMMA hydrogel) compared to pristine PPy.[145] In summary, the shift in the peaks is due to the strong intermolecular interaction between the components of the hydrogel and PPy chains.[138]

8.3.5. CHARACTERIZATION OF THE MORPHOLOGY OF THE CNC/PPy/GGMMA HYDROGEL

The SEM micrographs of the surface and cross-sectional morphology of the freeze-dried hydrogels are shown in **Figure 22**. Due to the freezing of water and the sublimation of ice crystals during freeze-drying, it is suggested that the physicochemical properties of hydrogels, particularly the microstructures could get changed.[146] Notwithstanding, the freeze-dried hydrogels exhibited a 3D microporous foam-like network structure typical of hydrogels reported in the literature.[85,137]

(a)

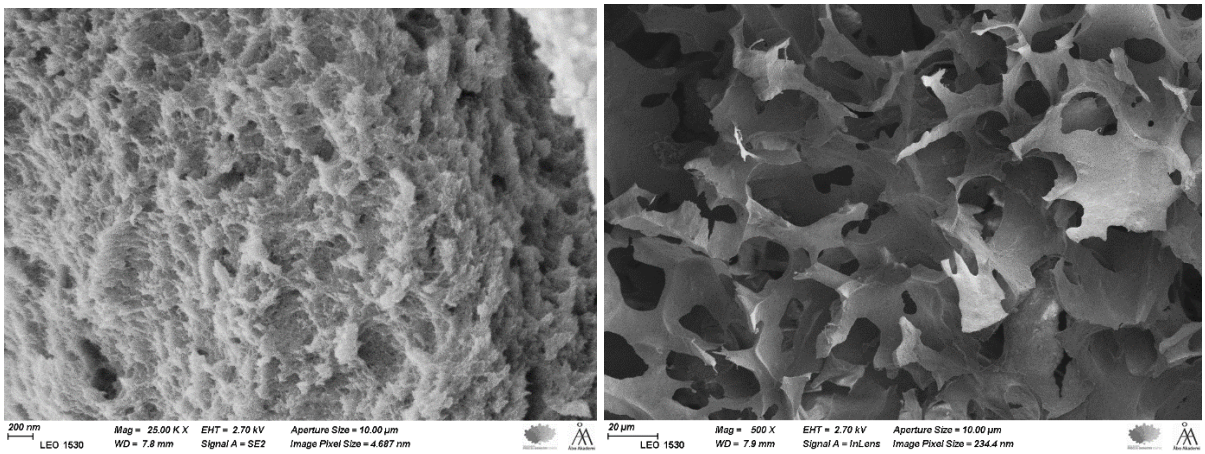

(b)

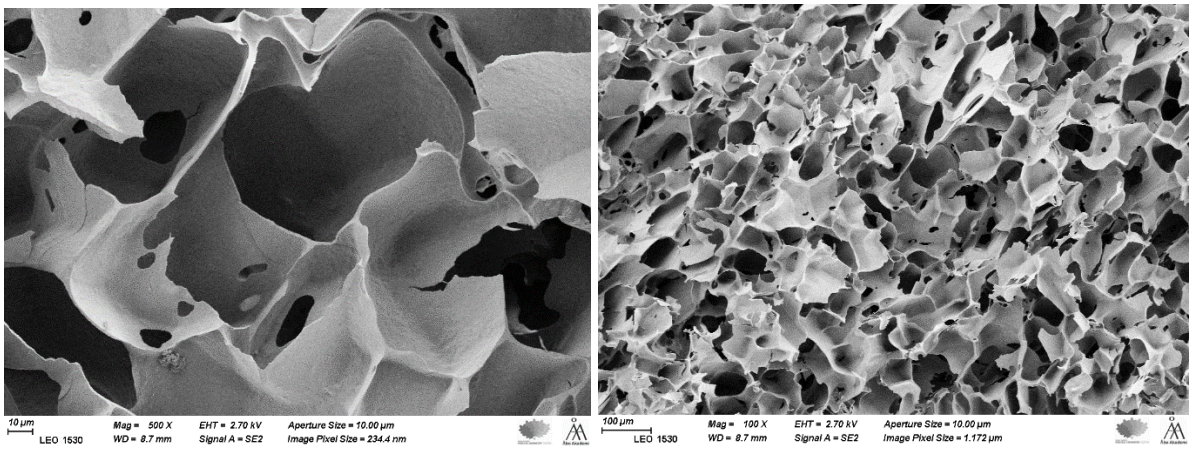

Figure 22. SEM micrographs of the CNC/PPy-3/GGMMA hydrogel, (a) surface morphology (b) cross-sectional morphology, with two different magnifications.

As shown in **Figure 22**, the microporous structures consist of interconnected pores which can reduce the distance which molecules need to pass through thus ensuring fast diffusion of molecules inside the pores. The pores allow for cell migration and proliferation, diffusion of oxygen, transport of nutrients and wastes, and vascularization.[85,137,147,148] Hence, the good porosity shown by the hydrogels implies that the growth of cells would not be inhibited, since the cells could readily spread and proliferate following their encapsulation within the hydrogel.

8.3.6. ELECTROCHEMICAL CHARACTERIZATIONS

The electrical conductivity of the hydrogels is an important factor especially in cardiac, neural, and muscle tissue engineering applications. Electrical conductivity improves cell-to-cell signaling, which in turn facilitates cellular growth, viability, and function.[149]

The electrochemical analyses were done for the CNC/PPy/GGMMA hydrogel ink (1 wt% CNC/PPy-3 + 6 wt% GGMMA + 0.5 wt% LAP) and without PPy (6 wt% GGMMA + 0.5 wt% LAP). The working electrode was prepared by drop-casting 10 µl of the hydrogel ink onto the Pt electrode. The analyses were initially performed without crosslinking the sample on the electrode surface. However, it was observed that the sample was not stable in the aqueous electrolyte for the duration of the analysis. The sample gradually disintegrated from the surface of the electrode during the analysis.

To hinder the disintegration of the sample, the CNC/PPy/GGMMA hydrogel ink on the coated electrode was UV irradiated at 365 nm to crosslink the hydrogel. The hydrogel was formed on the electrode surface after 2 min, and this was confirmed by tilting the electrode horizontally to check if the ink flows off the electrode surface. In this way, the hydrogel remained well-attached on the electrode surface and was stable during the electrochemical experiments. This approach of fabricating hydrogels on the electrode surface was adopted based on the method reported by previous studies.[85,120,150,151]

8.3.6a. ANALYSIS OF HYDROGEL ELECTROCHEMICAL STABILITY

Cyclic voltammetry (CV) is a powerful technique used to investigate electrochemical processes, and it has been applied in the characterization of conductive polymers and hydrogels for tissue engineering.[85,119,152] For application as a long-term implant in tissue engineering, CV is more gainfully employed in the assessment of the electrochemical stability by subjecting the

polymer-coated electrode to continuous potential cycling to determine the changes in the current-carrying capacity as time progresses.[119,152]

The electrochemical properties of the hydrogels with and without PPy were investigated with CV from -0.4 V to 0.4 V in 0.5 M KCl aqueous electrolyte solution. The CVs shown in **Figure 23 and Figure 24** are for the measurements performed at a scan rate of 20 mV/s. These CVs are similar to the CVs at a scan rate of 10 mV/s shown in **Appendix D**. The rectangular shape of the CV shown in **Figure 23** is characteristic of capacitive currents due to non-faradaic processes.[93,153]

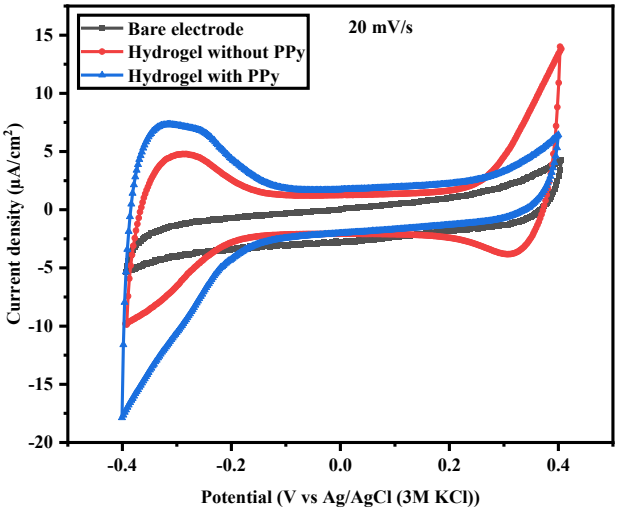

Figure 23. Cyclic voltammogram of the bare Pt electrode, hydrogel without PPy (6 wt% GGMMA + 0.5 wt% LAP), and hydrogel with PPy (1 wt% CNC/PPy-3 + 6 wt% GGMMA + 0.5 wt% LAP) in 0.5 M KCl at a scan rate of 20 mV/s.

As shown in **Figure 23**, there is a small increase in current for the electrode coated with the hydrogel containing PPy when compared to the bare Pt electrode. The increase in current can be attributed to the presence of PPy in the hydrogel. Also, during the 5 potential cycles used in the CV measurement, the hydrogel with PPy showed good electrochemical stability and charge carrying capacity as shown in **Figure 24.**

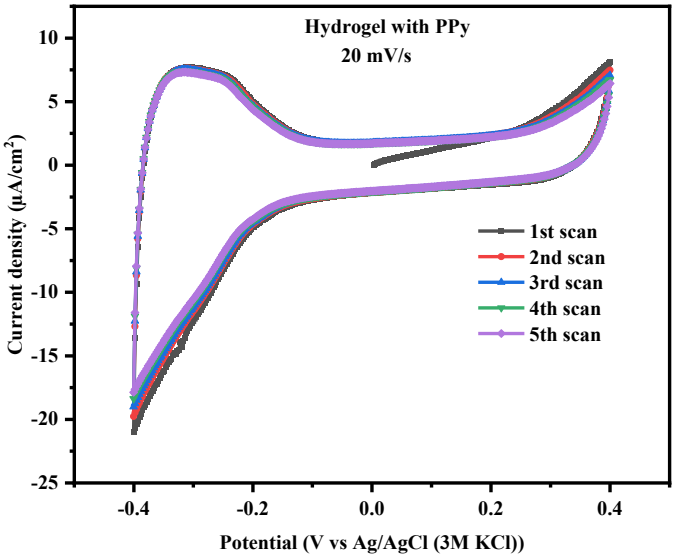

Figure 24. Cyclic voltammogram of the five potential cycles for the hydrogel with PPy (1 wt% CNC/PPy-3 + 6 wt% GGMMA + 0.5 wt% LAP) in 0.5 M KCl at a scan rate of 20 mV/s.

8.3.6b. ANALYSIS OF HYDROGEL ELECTROACTIVITY AND ELECTROCONDUCTIVITY

It has been shown that ion transport in electrically excitable tissues naturally occurs at a specific range of frequencies and in a bidirectional, alternating fashion.[154] Therefore, electrochemical impedance spectroscopy (EIS) measurements which are made under similar conditions to the cell culture environment are more relevant to *in vitro* investigations of cell behavior than are measurements of conductivity obtained by techniques such as the four-point probe method.[12] Hence, EIS which accounts for electron transfer from capacitive and resistive effects was used to characterize the conductivity and electroactivity of the hydrogels in an aqueous solution of 0.5 M KCl.

The results are shown for one of the replicates, while the other nine are shown in **Appendix E**. The Nyquist plots **(Figure 25)** for the hydrogels show a straight line with a phase angle higher than 45° (Warburg semi-infinite linear diffusion) but less than 90° (Warburg finite-length diffusion). This deviation from the classical 45° line for semi-infinite Warburg diffusion can be best attributed to a capacitive behavior such as a double-layer capacitance at the

electrode/hydrogel interface, where the vertical line is slightly tilted (constant phase angle) due to possible heterogeneities at the electrode/hydrogel interface.[122,155,156]

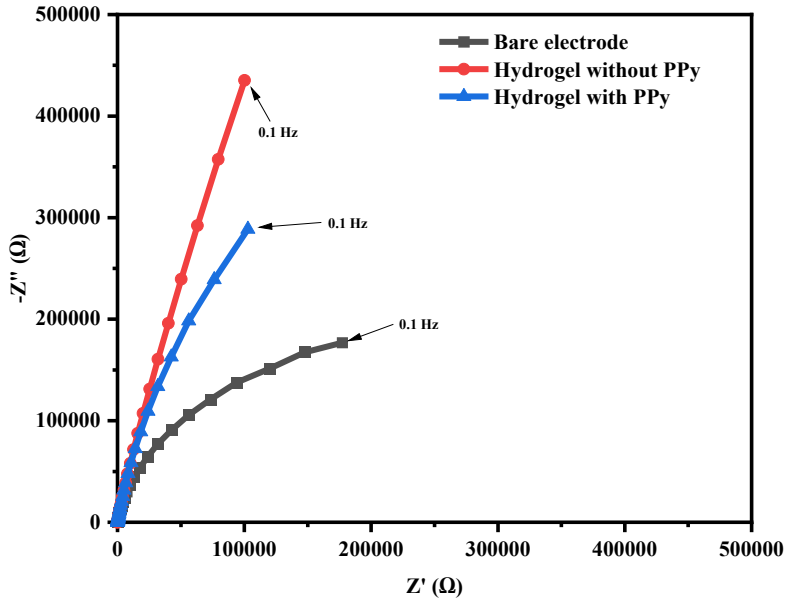

Figure 25. Nyquist plots of the bare Pt electrode, hydrogel without PPy (6 wt% GGMMA + 0.5 wt% LAP), and hydrogel with PPy (1 wt% CNC/PPy-3 + 6 wt% GGMMA + 0.5 wt% LAP) in 0.5 M KCl at E_{dc} of 0 V, E_{ac} of 10 mV, and frequency range from 0.1 Hz to 100 kHz.

Several electrical circuits were tested with the inbuilt NOVA analysis software which exploits a nonlinear least square regression to fit the data using the Levenberg–Marquardt algorithm. It works by changing the values of the parameters until the mathematical function matches the experimental data within a certain error margin and the quality of the fit is represented by the χ^2 (chi-squared) value. The equivalent circuit shown in **Figure 26** was found to give excellent fits for the experimental data. The average error (χ^2) of the fits for 10 different impedance spectra of hydrogels with and without PPy is shown in **Table 5.**

Figure 26. The equivalent electrical circuit for the hydrogels.

As can be seen in **Figure 26,** the model is composed of a resistor in series with a constant phase element (CPE). The resistor element accounts for the solution resistance (the high-frequency intersection with the Z' axis) and strongly depends on the electrolyte concentration.[155] CPE was used in the equivalent circuit model instead of capacitors, as is commonly done when the

capacitive elements of a system are imperfect.[157] The use of CPE improved the quality of the fit significantly. The CPE element in the electrical circuits accounts for the capacitive current observed in the cyclic voltammogram. This is confirmed by studies that the electrical characteristic of an electrical double layer, which produces the non-faradaic current, does not behave as an ideal capacitor but rather acts as a CPE.[158] The CPE can be determined mathematically with **Equation 7.**[159]

$$\vec{Z}_{CPE} = \frac{1}{Q_0(j\omega)^{\alpha}} \qquad \textbf{Equation 7}$$

Where ω is the angular frequency, $j = (-1)^{½}$, Q_0 is the magnitude of $1/Z_{CPE}$ (Y_{CPE}) at $\omega = 1$ rad/s, and the dispersion coefficient, α, obtains values between 0 and 1. When $\alpha = 1$, the CPE shows limiting behavior as a capacitor, and when α is equal to 0.5, the CPE shows limiting behavior as a Warburg element. At the opposite limit, $\alpha = 0$, CPE represents pure resistor. Although several concepts, such as surface roughness and non-uniform current distribution, have been proposed to account for the non-ideal behavior of the double layer, α is usually treated as an empirical constant with no real physical basis.

Table 5. Data for the equivalent electrical circuit elements after fitting, and the magnitude of impedance (*/Z/*) at various frequencies obtained from the impedance spectra

Element	Hydrogel without PPy	Hydrogel with PPy
R (Ω)[a]	33.54 ± 0.21	33.4 ± 0.7
Q_0 (Ss^{α})[a]	3.40 ± 0.14	4.42 ± 0.19
α[a]	0.9047 ± 0.0038	0.920 ± 0.006
χ^2	0.5	0.6
$\|Z\|$ at 1 Hz (kΩ)[a]	56.9 ± 1.9	43.3 ± 1.5
$\|Z\|$ at 1 kHz (Ω)[a]	113.4 ± 0.6	79.9 ± 2.2

[a]Each value represents an average of 10 measurements, and the confidence intervals are the repeatability standard deviation.

As shown in **Table 5,** the relatively high values of α indicate that the CPE can be considered to have largely a capacitive nature, which agrees with the CV.

A closer inspection of the plots in **Figure 25 and Appendix E** at low frequencies (down to 0.1 Hz) shows that the Nyquist plots for the bare Pt electrode and the electrode coated by the hydrogel with PPy deviate from the constant phase angle, forming the beginning of a semicircle. It is expected that this semicircle will become more prominent at lower frequencies down to 0.01 Hz. According to an earlier study by Bobacka et al.[155], this low-frequency process depends on the oxygen content of the solution and E_{dc}. They further reported that this low-frequency process is most probably due to a faradaic reaction at the electrode in parallel with the doping process, due to traces of oxygen in the solution. These findings at the low-frequency region are in agreement with the study of Vorotyntsev et al.[160] which takes into account both ion and electron transfer between the polymer and solution. Since this process is only observed in the hydrogel with PPy, it is evidence of its enhanced electroactivity due to the presence of PPy.

From the Bode plot (**Figure 27**) and as outlined in **Table 5**, at low frequencies similar to those in electroactive biological tissues (1 Hz), the hydrogel with PPy had lower impedance than the hydrogel without PPy and this is due to the better electron transfer kinetics in the system which can be attributed to the presence of PPy.[154] At 1 Hz, the impedance decreased from 56.9 ± 1.9 kΩ for the hydrogel without PPy to 43.3 ± 1.5 kΩ for the hydrogel with PPy.

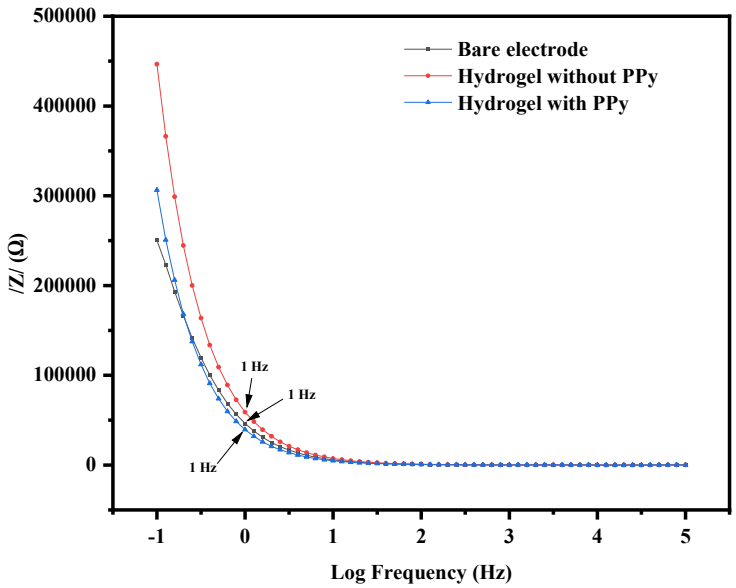

Figure 27. Bode plots of the bare Pt electrode, hydrogel without PPy (6 wt% GGMMA + 0.5 wt% LAP), and hydrogel with PPy (1 wt% CNC/PPy-3 + 6 wt% GGMMA + 0.5 wt% LAP) in 0.5 M KCl at E_{dc} of 0 V, E_{ac} of 10 mV, and frequency range from 0.1 Hz to 100 kHz.

Furthermore, the impedance at 1 kHz was examined because most neural cell communication occurs between 300 Hz and 1 kHz.[85,152] At 1 kHz, the impedance decreased from 113.4 ± 0.6 Ω for the hydrogel without PPy to 79.9 ± 2.2 Ω for the hydrogel with PPy. Also, the latest studies into the use of hydrogel scaffolds through which conducting polymers are deposited have shown that there is a significant increase in the surface area resulting in a reduction in impedance from ∼1 MΩ on a bare gold electrode to 7 kΩ for PPy/PSS-coated electrodes.[152] Hence, based on the EIS results, the reduction in impedance from 46.4 kΩ (1 Hz) and 91.5 Ω (1 kHz) in the bare Pt electrode to 43.3 ± 1.5 kΩ (1 Hz) and 79.9 ± 2.2 Ω (1 kHz) in the electrode coated with PPy-based hydrogel could be attributed to the conductive PPy in the hydrogel. The low impedance is beneficial for *in vivo* rapid cell-to-cell communication by endogenous bioelectrical signals produced by the activity of ion channels and pumps between neighboring cells and for efficient charge transfer from the electrode to cellular tissues *in vitro*.[12,85] Although, the reduction in impedance is relatively small, these results confirm the enhanced electroconductivity of the hydrogel containing PPy.

9. CONCLUSIONS

The goal of this project was to develop a biocompatible, electroconductive, and 3D printable hybrid hydrogel for tissue engineering. To achieve these goals, three different methods were explored to synthesize the composite biomaterials which constitute the hydrogel inks.

The CNC/PPy composite formed with the third method at a concentration of 1 wt% and 2 wt% of CNC showed good colloidal stability and sufficient electrostatic repulsion to prevent aggregation of the particles. This was due to the presence of a sufficient amount of sulfate half-ester groups on the surface of CNC after the chemical polymerization of PPy. Accordingly, the hydrogel inks fabricated with this composite possessed promising properties for high-quality 3D printing. After checking the conducting properties of the CNC/PPy/GGMMA hydrogel inks with the two-point probe method, a response was obtained on the multimeter for the hydrogel ink formulated with 1 wt% CNC and 0.2 M Py (CNC/PPy-3). The hydrogel formed with this sample (1 wt% CNC/PPy-3 + 6 wt% GGMMA) also showed lower impedance at physiologically relevant frequencies (1 Hz and 1000 Hz) when compared with the hydrogel without PPy and the bare Pt electrode.

On the other hand, the hydrogel inks formed with the first and second methods were not suitable for 3D printing due to the aggregation of the particles and low colloidal stability in solutions.

It was discovered that the combination of PVP and GelMA contributed to the large particle sizes via the reduction in electrostatic repulsion of the charges on the surface of CNC which led to the drop in colloidal stability and aggregation of particles. The low colloidal stability of the particles in the hydrogel inks could affect the resolution and precision of the tissue scaffold structures during 3D printing.

The findings of this investigation complement those of earlier studies, and it also has significant implications for the understanding of how the interactions of different materials in a composite and the synthesis conditions can influence the final properties of the hybrid material. Whilst this study did not confirm the biodegradability and biocompatibility of the hydrogel formed with the third method, it did partially validate the potential suitability of the hydrogel composed of CNC, PPy, and GGMMA for high-quality 3D printing and fabrication of tissue constructs for regeneration of electrically excitable tissues.

10. FUTURE PERSPECTIVES

This project was set out to fabricate an electroconductive hydrogel of 3D printing formulation for tissue engineering application. A natural progression of this work is to test the suitability of the hydrogel inks with direct ink writing 3D printing and encapsulate cells in the hydrogel to assess their viability. In future research, it could be worthwhile to explore a better setup for a more representative electrochemical characterization of the hydrogels. For example, the CV measurement in this thesis did not show any increase in current for the hydrogel with PPy. Previous studies have shown that in the electrochemical characterization of hydrogels, the passage of ions through the hydrogel and its thickness as well as placement and geometry of the electrodes are key factors. In literature, a predominant approach for the EIS analysis of hydrogels with varying composition is to insert the hydrogel in between two electrodes (e.g. gold-coated glass slides or stainless steel mesh electrodes) in one cell. The hydrogel is usually held with a clip to maintain a constant distance between the electrodes.[154,161] Another reported approach is the use of a Pt wire mesh which was inserted into the hydrogel in a three-electrode setup.[162] When such setups are used, the performed measurements focus on the changes in the impedance rendered by, for instance, different cross-linkers and residual charged monomers. Therefore, a different setup is needed to fully understand the electrochemical implications of the different components of the fabricated hydrogel.

Furthermore, considering that the hydrogel is meant to be a temporary scaffold for the delivery and integration of cells and/or growth factors at the repair site, further research is required to establish the biodegradability of the hydrogel because, in reconstructive medicine, degradability must be predictable so that tissue regeneration occurs at a rate that matches the degradation of the scaffold.[34] Also, considering the potential application of the hydrogel, further research could usefully explore the EIS response of the hydrogel in a phosphate-buffered saline solution which is more commonly used in biological research due to its similarity with physiological conditions.[154]

Finally, since the coating of PPy on the negatively charged CNC reduces the electrostatic repulsion required to maintain colloidal stability and prevent particle aggregation, it could be worthwhile to explore the use of PEDOT:PSS as the conductive polymer. Since GGMMA does not affect electrostatic repulsion, the comparatively higher conductivity of PEDOT:PSS could produce better results.

11. REFERENCES

1. Charles A Janeway, J., Travers, P., Walport, M. & Shlomchik, M. J. Responses to alloantigens and transplant rejection. *Immunobiol. Immune Syst. Health Dis. 5th Ed.* (2001).
2. Ahlmann, E., Patzakis, M., Roidis, N., Shepherd, L. & Holtom, P. Comparison of Anterior and Posterior Iliac Crest Bone Grafts in Terms of Harvest-Site Morbidity and Functional Outcomes. *JBJS* **84**, 716–720 (2002).
3. Vijayavenkataraman, S., Yan, W.-C., Lu, W. F., Wang, C.-H. & Fuh, J. Y. H. 3D bioprinting of tissues and organs for regenerative medicine. *Adv. Drug Deliv. Rev.* **132**, 296–332 (2018).
4. Ashammakhi, N., Ahadian, S., Xu, C., Montazerian, H., Ko, H., Nasiri, R., Barros, N. & Khademhosseini, A. Bioinks and bioprinting technologies to make heterogeneous and biomimetic tissue constructs. *Mater. Today Bio* **1**, 100008 (2019).
5. Davidenko, N., Schuster, C., Bax, D. V., Farndale, R. W., Hamaia, S., Best, S. M. Cameron, R. E. Evaluation of cell binding to collagen and gelatin: a study of the effect of 2D and 3D architecture and surface chemistry. *J. Mater. Sci. Mater. Med.* **27**, 148 (2016).
6. Ludwig, P. E., Huff, T. J. & Zuniga, J. M. The potential role of bioengineering and three-dimensional printing in curing global corneal blindness. *J. Tissue Eng.* **9**, 2041731418769863 (2018).
7. Xing, Q., Yates, K., Vogt, C., Qian, Z., Frost, M. C. & Zhao, F. Increasing Mechanical Strength of Gelatin Hydrogels by Divalent Metal Ion Removal. *Sci. Rep.* **4**, 4706 (2014).
8. Dash, R., Foston, M. & Ragauskas, A. J. Improving the mechanical and thermal properties of gelatin hydrogels cross-linked by cellulose nanowhiskers. *Carbohydr. Polym.* **91**, 638–645 (2013).
9. Qazi, T. H., Rai, R. & Boccaccini, A. R. Tissue engineering of electrically responsive tissues using polyaniline based polymers: A review. *Biomaterials* **35**, 9068–9086 (2014).
10. Hardy, J. G., Lee, J. Y. & Schmidt, C. E. Biomimetic conducting polymer-based tissue scaffolds. *Curr. Opin. Biotechnol.* **24**, 847–854 (2013).

11. Leppik, L., Oliveira, K. M. C., Bhavsar, M. B. & Barker, J. H. Electrical stimulation in bone tissue engineering treatments. *Eur. J. Trauma Emerg. Surg.* **46**, 231–244 (2020).

12. Breukers, R. D., Gilmore, K. J., Kita, M., Wagner, K. K., Higgins, M. J., Moulton, S. E., Clark, G. M., Officer, D. L., Kapsa, R. M. I. & Wallace, G. G. Creating conductive structures for cell growth: Growth and alignment of myogenic cell types on polythiophenes. *J. Biomed. Mater. Res. A* **95A**, 256–268 (2010).

13. Sun, B., Wu, T., Wang, J., Li, D., Wang, J., Gao, Q., Bhutto, M. A., El-Hamshary, H., Al-Deyab, S. S. & Mo, X. Polypyrrole-coated poly(L-lactic acid-co-ε-caprolactone)/silk fibroin nanofibrous membranes promoting neural cell proliferation and differentiation with electrical stimulation. *J. Mater. Chem. B* **4**, 6670–6679 (2016).

14. Navaei, A., Saini, H., Christenson, W., Sullivan, R. T., Ros, R. & Nikkhah, M. Gold nanorod-incorporated gelatin-based conductive hydrogels for engineering cardiac tissue constructs. *Acta Biomater.* **41**, 133–146 (2016).

15. Harrison, B. S. & Atala, A. Carbon nanotube applications for tissue engineering. *Biomaterials* **28**, 344–353 (2007).

16. Ketabat, F., Karkhaneh, A., Aghdam, R. M. & Tafti, S. H. A. Injectable conductive collagen/alginate/polypyrrole hydrogels as a biocompatible system for biomedical applications. *J. Biomater. Sci. Polym. Ed.* **28**, 794–805 (2017).

17. Sista, P., Ghosh, K., Martinez, J. S. & Rocha, R. C. Polythiophenes in biological applications. *J. Nanosci. Nanotechnol.* **14**, 250–272 (2014).

18. Sultana, N., Chang, H. C., Jefferson, S. & Daniels, D. E. Application of conductive poly(3,4-ethylenedioxythiophene):poly(styrenesulfonate) (PEDOT:PSS) polymers in potential biomedical engineering. *J. Pharm. Investig.* **50**, 437–444 (2020).

19. Liang, Y. & Goh, J. C.-H. Polypyrrole-Incorporated Conducting Constructs for Tissue Engineering Applications: A Review. *Bioelectricity* **2**, 101–119 (2020).

20. Spearman, B. S., Hodge, A. J., Porter, J. L., Hardy, J. G., Davis, Z. D., Xu, T., Zhang, X., Schmidt, C. E., Hamilton, M. C. & Lipke, E. A. Conductive interpenetrating networks of

polypyrrole and polycaprolactone encourage electrophysiological development of cardiac cells. *Acta Biomater.* **28**, 109–120 (2015).

21. Ateh, D. d, Navsaria, H. a & Vadgama, P. Polypyrrole-based conducting polymers and interactions with biological tissues. *J. R. Soc. Interface* **3**, 741–752 (2006).
22. Guiseppi-Elie, A. Electroconductive hydrogels: Synthesis, characterization and biomedical applications. *Biomaterials* **31**, 2701–2716 (2010).
23. Hammerick, K. E., Longaker, M. T. & Prinz, F. B. In vitro effects of direct current electric fields on adipose-derived stromal cells. *Biochem. Biophys. Res. Commun.* **397**, 12–17 (2010).
24. Wu, Y., Chen, Y. X., Yan, J., Quinn, D., Dong, P., Sawyer, S. W. & Soman, P. Fabrication of conductive gelatin methacrylate–polyaniline hydrogels. *Acta Biomater.* **33**, 122–130 (2016).
25. Wang, S., Lei, J., Yi, X., Yuan, L., Ge, L., Li, D. & Mu, C. Fabrication of Polypyrrole-Grafted Gelatin-Based Hydrogel with Conductive, Self-Healing, and Injectable Properties. *ACS Appl. Polym. Mater.* **2**, 3016–3023 (2020).
26. Mondal, S. Review on Nanocellulose Polymer Nanocomposites. *Polym.-Plast. Technol. Eng.* **57**, 1377–1391 (2018).
27. Nascimento, D. M., Nunes, Y. L., Figueiredo, M. C. B., de Azeredo, H. M. C., Aouada, F. A., Feitosa, J. P. A., Rosa, M. F. & Dufresne, A. Nanocellulose nanocomposite hydrogels: technological and environmental issues. *Green Chem.* **20**, 2428–2448 (2018).
28. Osorio-Madrazo, A., Eder, M., Rueggeberg, M., Pandey, J. K., Harrington, M. J., Nishiyama, Y., Putaux, J., Rochas, C. & Burgert, C. Reorientation of Cellulose Nanowhiskers in Agarose Hydrogels under Tensile Loading. *Biomacromolecules* **13**, 850–856 (2012).
29. Zhang, X., Huang, J., Chang, P. R., Li, J., Chen, Y., Wang, D., Yu, J. & Chen, J. Structure and properties of polysaccharide nanocrystal-doped supramolecular hydrogels based on Cyclodextrin inclusion. *Polymer* **51**, 4398–4407 (2010).
30. Zhang, X., Morits, M., Jonkergouw, C., Ora, A., Valle-Delgado, J. J., Farooq, M., Ajdary, R., Huan, S., Linder, M., Rojas, O., Sipponen, M. H. & Österberg, M. Three-Dimensional Printed Cell Culture Model Based on Spherical Colloidal Lignin Particles and Cellulose Nanofibril-Alginate Hydrogel. *Biomacromolecules* **21**, 1875–1885 (2020).

31. Zeng, M. & Zhang, Y. Colloidal nanoparticle inks for printing functional devices: emerging trends and future prospects. *J. Mater. Chem. A* **7**, 23301–23336 (2019).

32. Xu, W., Wang, X., Sandler, N., Willför, S. & Xu, C. Three-Dimensional Printing of Wood-Derived Biopolymers: A Review Focused on Biomedical Applications. *ACS Sustain. Chem. Eng.* **6**, 5663–5680 (2018).

33. Eltom, A., Zhong, G. & Muhammad, A. Scaffold Techniques and Designs in Tissue Engineering Functions and Purposes: A Review. *Advances in Materials Science and Engineering* vol. 2019 e3429527

34. Velema, J. & Kaplan, D. Biopolymer-Based Biomaterials as Scaffolds for Tissue Engineering. in *Tissue Engineering I* (eds. Lee, K. & Kaplan, D.) 187–238 (Springer, 2006).

35. Witzler, M., Alzagameem, A., Bergs, M., El Khaldi-Hansen, B., Klein, S. E., Hielscher, D., Kamm, B., Kreyenschmidt, J., Tobiasch, E. & Schulze, M. Lignin-Derived Biomaterials for Drug Release and Tissue Engineering. *Mol. Basel Switz.* **23**, (2018).

36. Zhu, H., Luo, W., Ciesielski, P. N., Fang, Z., Zhu, J. Y., Henriksson, G., Himmel, M. E. & Hu, L. Wood-Derived Materials for Green Electronics, Biological Devices, and Energy Applications. *Chem. Rev.* **116**, 9305–9374 (2016).

37. Börjesson, M. & Westman, G. Crystalline Nanocellulose — Preparation, Modification, and Properties. *Cellul. - Fundam. Asp. Curr. Trends* (2015).

38. Roy, D., Semsarilar, M., Guthrie, J. T. & Perrier, S. Cellulose modification by polymer grafting: a review. *Chem. Soc. Rev.* **38**, 2046–2064 (2009).

39. Dias, O. A. T., Konar, S., Leao, A. L., Yang, W., Tjong, J. & Sain, M. Current State of Applications of Nanocellulose in Flexible Energy and Electronic Devices. *Front. Chem.* **8**, (2020).

40. Foster, E. J., Moon, R. J., Agarwal, U. P., Bortner, M. J., Bras, J., Camarero-Espinosa, S., Chan, K. J., Clift, M. J. D., Cranston, E. D., Eichhorn, S. J., Fox, D. M., Hamad, W. Y., Heux, L., Jean, B., Korey, M., Nieh, W., Ong, K. J., Reid, M. S., Renneckar, S., Roberts, R., Shatkin, J. A., Simonsen, J., Stinson-Bagby, K., Wanasekaraq, N. & Youngbloodl, J. Current characterization methods for cellulose nanomaterials. *Chem. Soc. Rev.* **47**, 2609–2679 (2018).

41. Habibi, Y. Key advances in the chemical modification of nanocelluloses. *Chem. Soc. Rev.* **43**, 1519–1542 (2014).

42. Yang, X. & Cranston, E. D. Chemically Cross-Linked Cellulose Nanocrystal Aerogels with Shape Recovery and Superabsorbent Properties. *Chem. Mater.* **26**, 6016–6025 (2014).

43. Yang, J. & Han, C. Mechanically Viscoelastic Properties of Cellulose Nanocrystals Skeleton Reinforced Hierarchical Composite Hydrogels. *ACS Appl. Mater. Interfaces* **8**, 25621–25630 (2016).

44. Huang, S., Liu, X., Chang, C. & Wang, Y. Recent developments and prospective food-related applications of cellulose nanocrystals: a review. *Cellulose* **27**, 2991–3011 (2020).

45. He, X., Xiao, Q., Lu, C., Wang, Y., Zhang, X., Zhao, J., Zhang, W., Zhang, X. & Deng, Y. Uniaxially aligned electrospun all-cellulose nanocomposite nanofibers reinforced with cellulose nanocrystals: scaffold for tissue engineering. *Biomacromolecules* **15**, 618–627 (2014).

46. Köhnke, T., Lin, A., Elder, T., Theliander, H. & Ragauskas, A. J. Nanoreinforced xylan–cellulose composite foams by freeze-casting. *Green Chem.* **14**, 1864 (2012).

47. Dugan, J. M., Gough, J. E. & Eichhorn, S. J. Directing the Morphology and Differentiation of Skeletal Muscle Cells Using Oriented Cellulose Nanowhiskers. *Biomacromolecules* **11**, 2498–2504 (2010).

48. Brinchi, L., Cotana, F., Fortunati, E. & Kenny, J. M. Production of nanocrystalline cellulose from lignocellulosic biomass: technology and applications. *Carbohydr. Polym.* **94**, 154–169 (2013).

49. Camarero Espinosa, S., Kuhnt, T., Foster, E. J. & Weder, C. Isolation of thermally stable cellulose nanocrystals by phosphoric acid hydrolysis. *Biomacromolecules* **14**, 1223–1230 (2013).

50. Amin, K. N. M., Annamalai, P. K., Morrow, I. C. & Martin, D. Production of cellulose nanocrystals via a scalable mechanical method. *RSC Adv.* **5**, 57133–57140 (2015).

51. Lu, P. & Hsieh, Y.-L. Preparation and characterization of cellulose nanocrystals from rice straw. *Carbohydr. Polym.* **87**, 564–573 (2012).

52. Roman, M. & Winter, W. T. Effect of sulfate groups from sulfuric acid hydrolysis on the thermal degradation behavior of bacterial cellulose. *Biomacromolecules* **5**, 1671–1677 (2004).

53. Kandhola, G., Djioleu, A., Rajan, K., Labbé, N., Sakon, J., Carrier, D. J. & Kim, J. Maximizing production of cellulose nanocrystals and nanofibers from pre-extracted loblolly pine kraft pulp: a response surface approach. *Bioresour. Bioprocess.* **7**, 19 (2020).

54. Deepa, B., Abraham, E., Cherian, B. M., Bismarck, A., Blaker, J. J., Pothan, L. A., Leao, A. L., de Souza, S. F. & Kottaisamy, M. Structure, morphology and thermal characteristics of banana nano fibers obtained by steam explosion. *Bioresour. Technol.* **102**, 1988–1997 (2011).

55. Aguayo, M. G., Pérez, A. F., Reyes, G., Oviedo, C., Gacitúa, W., Gonzalez, R. & Uyarte, O. Isolation and Characterization of Cellulose Nanocrystals from Rejected Fibers Originated in the Kraft Pulping Process. *Polymers* **10**, (2018).

56. Zergane, H., Abdi, S., Xu, H., Hemming, J., Wang, X., Willför, S. & Habibi, Y. Ampelodesmos mauritanicus a new sustainable source for nanocellulose substrates. *Ind. Crops Prod.* **144**, 112044 (2020).

57. Mishra, R. K., Sabu, A. & Tiwari, S. K. Materials chemistry and the futurist eco-friendly applications of nanocellulose: Status and prospect. *J. Saudi Chem. Soc.* **22**, 949–978 (2018).

58. Heise, K., Kontturi, E., Allahverdiyeva, Y., Tammelin, T., Linder, M. B., Nonappa & Ikkala, O. Nanocellulose: Recent Fundamental Advances and Emerging Biological and Biomimicking Applications. *Adv. Mater.* **33**, 2004349 (2021).

59. Barhoum, A., Li, H., Chen, M., Cheng, L., Yang, W. & Dufresne, A. Emerging Applications of Cellulose Nanofibers. in *Handbook of Nanofibers* (eds. Barhoum, A., Bechelany, M. & Makhlouf, A. S. H.) 1131–1156, Springer International Publishing (2019)

60. Peng, F., Peng, P., Xu, F. & Sun, R.-C. Fractional purification and bioconversion of hemicelluloses. *Biotechnol. Adv.* **30**, 879–903 (2012).

61. Hu, L., Fang, X., Du, M., Luo, F. & Guo, S. Hemicellulose-Based Polymers Processing and Application. *Am. J. Plant Sci.* **11**, 2066–2079 (2020).

62. Zhao, W., Glavas, L., Odelius, K., Edlund, U. & Albertsson, A.-C. Facile and Green Approach towards Electrically Conductive Hemicellulose Hydrogels with Tunable Conductivity and Swelling Behavior. *Chem. Mater.* **26**, 4265–4273 (2014).

63. Willför, S., Sjoholm, R., Laine, C., Roslund, C., Hemming, J. & Holmbom, B. Characterisation of water-soluble galactoglucomannans from Norway spruce wood and thermomechanical pulp. *Carbohydr. Polym.* **52**, 175–187 (2003).

64. Yu, C., Schimelman, J., Wang, P., Miller, K. L., Ma, X., You, S., Guan, J., Sun, B., Zhu, W. & Chen, S. Photopolymerizable Biomaterials and Light-Based 3D Printing Strategies for Biomedical Applications. *Chem. Rev.* (2020).

65. Felipe-Mendes, C., Ruiz-Rubio, L. & Vilas-Vilela, J. L. Biomaterials obtained by photopolymerization: from UV to two photon. *Emergent Mater.* **3**, 453–468 (2020).

66. Choi, G. & Cha, H. J. Recent advances in the development of nature-derived photocrosslinkable biomaterials for 3D printing in tissue engineering. *Biomater. Res.* **23**, 18 (2019).

67. Xu, W., Zhang, X., Yang, P., Långvik, O., Wang, X., Zhang, Y., Cheng, F., Österberg, M., Willför, S. & Xu, C. Surface Engineered Biomimetic Inks Based on UV Cross-Linkable Wood Biopolymers for 3D Printing. *ACS Appl. Mater. Interfaces* **11**, 12389–12400 (2019).

68. Fairbanks, B. D., Schwartz, M. P., Bowman, C. N. & Anseth, K. S. Photoinitiated polymerization of PEG-diacrylate with lithium phenyl-2,4,6-trimethylbenzoylphosphinate: polymerization rate and cytocompatibility. *Biomaterials* **30**, 6702–6707 (2009).

69. Sun, M., Sun, X., Wang, Z., Guo, S., Yu, G. & Yang, H. Synthesis and Properties of Gelatin Methacryloyl (GelMA) Hydrogels and Their Recent Applications in Load-Bearing Tissue. *Polymers* **10**, (2018).

70. Van Den Bulcke, A. I., Bogdanov, B., De Rooze, N., Schacht, E. H., Cornelissen, M. & Berghmans, H. Structural and Rheological Properties of Methacrylamide Modified Gelatin Hydrogels. *Biomacromolecules* **1**, 31–38 (2000).

71. Yue, K., Santiago, G. T., Alvarez, M. M., Tamayol, A., Annabi, N. & Khademhosseini, A. Synthesis, properties, and biomedical applications of gelatin methacryloyl (GelMA) hydrogels. *Biomaterials* **73**, 254–271 (2015).

72. Nichol, J. W., Koshy, S. T., Bae, H., Hwang, C. M., Yamanlar, S. & Khademhosseini, A. Cell-laden microengineered gelatin methacrylate hydrogels. *Biomaterials* **31**, 5536–5544 (2010).

73. Balint, R., Cassidy, N. J. & Cartmell, S. H. Conductive polymers: Towards a smart biomaterial for tissue engineering. *Acta Biomater.* **10**, 2341–2353 (2014).

74. Heinze, J., Frontana-Uribe, B. A. & Ludwigs, S. Electrochemistry of Conducting Polymers—Persistent Models and New Concepts. *Chem. Rev.* **110**, 4724–4771 (2010).

75. Wong, J. Y., Langer, R. & Ingber, D. E. Electrically conducting polymers can noninvasively control the shape and growth of mammalian cells. *Proc. Natl. Acad. Sci. U. S. A.* **91**, 3201–3204 (1994).

76. Lu, H., Zhang, N. & Ma, M. Electroconductive hydrogels for biomedical applications. *WIREs Nanomedicine Nanobiotechnology* **11**, e1568 (2019).

77. Saberi, A., Jabbari, F., Zarrintaj, P., Saeb, M. R. & Mozafari, M. Electrically Conductive Materials: Opportunities and Challenges in Tissue Engineering. *Biomolecules* **9**, (2019).

78. Gajendiran, M., Choi, J., Kim, S., Kim, K., Shin, H., Koo, H. & Kim, K. Conductive biomaterials for tissue engineering applications. *J. Ind. Eng. Chem.* **51**, 12–26 (2017).

79. Palza, H., Zapata, P. A. & Angulo-Pineda, C. Electroactive Smart Polymers for Biomedical Applications. *Mater. Basel Switz.* **12**, (2019).

80. Wise, D. L. *Electrical and Optical Polymer Systems: Fundamentals: Methods, and Applications*. (CRC Press, 1998).

81. Le, T.-H., Kim, Y. & Yoon, H. Electrical and Electrochemical Properties of Conducting Polymers. *Polymers* **9**, (2017).

82. MacDiarmid, A. G., Mammone, R. J., Kaner, R. B. & Porter, L. The concept of 'doping' of conducting polymers: the role of reduction potentials. *Philos. Trans. R. Soc. Lond. Ser. Math. Phys. Sci.* **314**, 3–15 (1985).

83. Al-Dulaimi, A. A. & Wanrosli, W. D. Preparation of Colloidal Properties and Water Dispersible Conductive Polypyrrole Nanocomposite of Nanocrystalline Cellulose. *Polym. Polym. Compos.* **24**, 695–702 (2016).

84. Al-Dulaimi, A. A. & Wan Rosli, W. D. Water Dispersion Conductive Polypyrrole Based on Nanocrystalline Cellulose. *Advanced Materials Research* vol. 1043 105–108, (2014).

85. Zhou, L., Fan, L., Yi, X., Zhou, Z., Liu, C., Fu, R., Dai, C., Wang, Z., Chen, X., Yu, P., Chen, D., Tan, G., Wang, Q. & Ning, C. Soft Conducting Polymer Hydrogels Cross-Linked and Doped by Tannic Acid for Spinal Cord Injury Repair. *ACS Nano* **12**, 10957–10967 (2018).

86. Wright, C. J., Molino, B. Z., Chung, J. H. Y., Pannell, J. T., Kuester, M., Molino, P. J. & Hanks, T. W. Synthesis and 3D Printing of Conducting Alginate–Polypyrrole Ionomers. *Gels* **6**, 13 (2020).

87. Tomczykowa, M. & Plonska-Brzezinska, M. E. Conducting Polymers, Hydrogels and Their Composites: Preparation, Properties and Bioapplications. *Polymers* **11**, 350 (2019).

88. Yang, S., Jang, L. K., Kim, S., Yang, J., Yang, K., Cho, S. & Lee, J. Y. Polypyrrole/Alginate Hybrid Hydrogels: Electrically Conductive and Soft Biomaterials for Human Mesenchymal Stem Cell Culture and Potential Neural Tissue Engineering Applications. *Macromol. Biosci.* **16**, 1653–1661 (2016).

89. Tan, Y. & Ghandi, K. Kinetics and mechanism of pyrrole chemical polymerization. *Synth. Met.* **175**, 183–191 (2013).

90. Andrieux, C. P., Audebert, P., Hapiot, P. & Saveant, J. M. Identification of the first steps of the electrochemical polymerization of pyrroles by means of fast potential step techniques. *J. Phys. Chem.* **95**, 10158–10164 (1991).

91. Yussuf, A., Al-Saleh, M., Al-Enezi, S. & Abraham, G. Synthesis and Characterization of Conductive Polypyrrole: The Influence of the Oxidants and Monomer on the Electrical, Thermal, and Morphological Properties. *Int. J. Polym. Sci.* **2018**, e4191747 (2018).

92. Armes, S. P. Optimum reaction conditions for the polymerization of pyrrole by iron(III) chloride in aqueous solution. *Synth. Met.* **20**, 365–371 (1987).

93. Wu, X., Chabot, V. L., Kim, B. K., Yu, A., Berry, R. M. & Tam, K. C. Cost-effective and Scalable Chemical Synthesis of Conductive Cellulose Nanocrystals for High-performance Supercapacitors. *Electrochimica Acta* **138**, 139–147 (2014).

94. Qi, Z. & Pickup, P. G. Size Control of Polypyrrole Particles. *Chem. Mater.* **9**, 2934–2939 (1997).

95. Wu, X., Tang, J., Duan, Y., Yu, A., Berry, R. M. & Tam, K. C. Conductive cellulose nanocrystals with high cycling stability for supercapacitor applications. *J. Mater. Chem. A* **2**, 19268–19274 (2014).

96. Abraham, J., Jose, B., Jose, A. & Thomas, S. Chapter 2 - Characterization of green nanoparticles from plants. in *Phytonanotechnology* (eds. Thajuddin, N. & Mathew, S.) 21–39 Elsevier, (2020).

97. Campbell, J., Burkitt, S., Dong, N. & Zavaleta, C. Chapter 9 - Nanoparticle characterization techniques. in *Nanoparticles for Biomedical Applications* (eds. Chung, E. J., Leon, L. & Rinaldi, C.) 129–144 Elsevier, (2020).

98. Foujdar, R., Bera, M. B. & Chopra, H. K. Chapter 30 - Phenolic nanoconjugates and its application in food. in *Biopolymer-Based Formulations* (eds. Pal, K. et al.) 751–780 Elsevier, (2020).

99. Barhoum, A., García-Betancourt, M. L., Rahier, H. & Van Assche, G. Chapter 9 - Physicochemical characterization of nanomaterials: polymorph, composition, wettability, and thermal stability. in *Emerging Applications of Nanoparticles and Architecture Nanostructures* (eds. Barhoum, A. & Makhlouf, A. S. H.) 255–278 Elsevier, (2018).

100. Berger Bioucas, F. E., Damm, C., Peukert, W., Rausch, M. H., Koller, T. M., Giraudet, C. & Fröba, A. P. Translational and Rotational Diffusion Coefficients of Gold Nanorods Dispersed in Mixtures of Water and Glycerol by Polarized Dynamic Light Scattering. *J. Phys. Chem. B* **123**, 9491–9502 (2019).

101. Meirelles, A. A. D., Costa, A. L. R. & Cunha, R. L. Cellulose nanocrystals from ultrasound process stabilizing O/W Pickering emulsion. *Int. J. Biol. Macromol.* **158**, 75–84 (2020).

102. Hoo, C. M., Starostin, N., West, P. & Mecartney, M. L. A comparison of atomic force microscopy (AFM) and dynamic light scattering (DLS) methods to characterize nanoparticle size distributions. *J. Nanoparticle Res.* **10**, 89–96 (2008).

103. Fissan, H., Ristig, S., Kaminski, H., Asbach, C. & Epple, M. Comparison of different characterization methods for nanoparticle dispersions before and after aerosolization. *Anal. Methods* **6**, 7324 (2014).

104. Mudalige, T., Qu, H., Haute, D. V., Ansar, S. M., Paredes, A. & Ingle, T. Chapter 11 - Characterization of Nanomaterials: Tools and Challenges. in *Nanomaterials for Food Applications* (eds. López Rubio, A., Fabra Rovira, M. J., martínez Sanz, M. & Gómez-Mascaraque, L. G.) 313–353 Elsevier, (2019).

105. Shi, Z., Gao, X., Ullah, M. W., Li, S., Wang, Q. & Yang, G. Electroconductive natural polymer-based hydrogels. *Biomaterials* **111**, 40–54 (2016).

106. Nasrazadani, S. & Hassani, S. Chapter 2 - Modern analytical techniques in failure analysis of aerospace, chemical, and oil and gas industries. in *Handbook of Materials Failure Analysis with Case Studies from the Oil and Gas Industry* (eds. Makhlouf, A. S. H. & Aliofkhazraei, M.) 39–54 (Butterworth-Heinemann, 2016).

107. Stinson-Bagby, K. L., Roberts, R. & Foster, E. J. Effective cellulose nanocrystal imaging using transmission electron microscopy. *Carbohydr. Polym.* **186**, 429–438 (2018).

108. Chalmers, J. M. INFRARED SPECTROSCOPY | Sample Presentation☆. in *Reference Module in Chemistry, Molecular Sciences and Chemical Engineering,* Elsevier, (2013).

109. Faghihzadeh, F., Anaya, N. M., Schifman, L. A. & Oyanedel-Craver, V. Fourier transform infrared spectroscopy to assess molecular-level changes in microorganisms exposed to nanoparticles. *Nanotechnol. Environ. Eng.* **1**, 1 (2016).

110. Calloway, D. Beer-Lambert Law. *J. Chem. Educ.* **74**, 744 (1997).

111. Patil, A., Heeger, A. J. & Wudl, F. Optical properties of conducting polymers. *Chem. Rev.* **88**, 1, 183–200 (1988).

112. Roncali, J. Synthetic Principles for Bandgap Control in Linear π-Conjugated Systems. *Chem. Rev.* **97**, 173–206 (1997).

113. Zhang, J., Zhang, H., Wu, J. & Zhang, J. Chapter 5 - Membrane/Ionomer Proton Conductivity Measurements. in *Pem Fuel Cell Testing and Diagnosis* (eds. Zhang, J., Zhang, H., Wu, J. & Zhang, J.) 143–170 Elsevier, (2013).

114. Dyer, S. A. *Wiley Survey of Instrumentation and Measurement*. John Wiley & Sons, (2004).

115. Li, M.-Y., Yang, M., Vargas, E., Neff, K., Vanli, A. & Liang, R. Analysis of variance on thickness and electrical conductivity measurements of carbon nanotube thin films. *Meas Sci Technol* 13 (2016).

116. Pletcher, D., Greff, R., Peat, R., Peter, L. M. & Robinson, J. *Instrumental Methods in Electrochemistry*, Ellis Horwood Limited, Southampton (1993) 179.

117. Wang, H., Sayed, S. Y., Luber, E. J., Olsen, B. C., Shirurkar, S. M., Venkatakrishnan, S., Tefashe, U. M., Farquhar, A. K., Smotkin, E. S., McCreery, R. L. & Buriak, J. M. Redox Flow Batteries: How to Determine Electrochemical Kinetic Parameters. *ACS Nano* **14**, 2575–2584 (2020).

118. Elgrishi, N., Rountree, K. J., McCarthy, B. D., Rountree, E. S., Eisenhart, T. T. & Dempsey, J. L. A Practical Beginner's Guide to Cyclic Voltammetry. *J. Chem. Educ.* **95**, 197–206 (2018).

119. Kleber, C., Bruns, M., Lienkamp, K., Rühe, J. & Asplund, M. An interpenetrating, microstructurable and covalently attached conducting polymer hydrogel for neural interfaces. *Acta Biomater.* **58**, 365–375 (2017).

120. Li, L., Ge, J., Ma, P. X. & Guo, B. Injectable conducting interpenetrating polymer network hydrogels from gelatin-graft-polyaniline and oxidized dextran with enhanced mechanical properties. *RSC Adv.* **5**, 92490–92498 (2015).

121. Shepherd, R. K., Villalobos, J., Burns, O. & Nayagam, D. A. X. The development of neural stimulators: a review of preclinical safety and efficacy studies. *J. Neural Eng.* **15**, 041004 (2018).

122. Randviir, E. P. & Banks, C. E. Electrochemical impedance spectroscopy: an overview of bioanalytical applications. *Anal. Methods* **5**, 1098–1115 (2013).

123. Benson, K., Cramer, S. & Galla, H.-J. Impedance-based cell monitoring: barrier properties and beyond. *Fluids Barriers CNS* **10**, 5 (2013).

124. Amini, M., Hisdal, J. & Kalvøy, H. Applications of bioimpedance measurement techniques in tissue engineering. *J. Electr. Bioimpedance* **9**, 142–158 (2018).

125. Bard, A. & Faulkner, L. R. *Electrochemical Methods: Fundamentals and Applications,* 2nd Edition, John Wiley & Sons, Inc. 605 Third Avenue, New York, NY 10158-0012, USA (2000) 386.

126. Kedzior, S. A., Marway, H. S. & Cranston, E. D. Tailoring Cellulose Nanocrystal and Surfactant Behavior in Miniemulsion Polymerization. *Macromolecules* **50**, 2645–2655 (2017).

127. Alam, K. M., Kar, P., Thakur, U, K., Kisslinger, R., Mahdi, N., Mohammadpour, A., Baheti, P. A., Kumar, P. & Shankar, K. Remarkable self-organization and unusual conductivity behavior in cellulose nanocrystal-PEDOT: PSS nanocomposites. *J. Mater. Sci. Mater. Electron.* **30**, 1390–1399 (2019).

128. Boluk, Y. & Danumah, C. Analysis of cellulose nanocrystal rod lengths by dynamic light scattering and electron microscopy. *J. Nanoparticle Res.* **16**, 2174 (2013).

129. Lam, S.-M., Kee, M.-W. & Sin, J.-C. Influence of PVP surfactant on the morphology and properties of ZnO micro/nanoflowers for dye mixtures and textile wastewater degradation. *Mater. Chem. Phys.* **212**, 35–43 (2018).

130. Rosická, D. & Šembera, J. Changes in the nanoparticle aggregation rate due to the additional effect of electrostatic and magnetic forces on mass transport coefficients. *Nanoscale Res. Lett.* **8**, 20 (2013).

131. Kariduraganavar, M. Y., Kittur, A. A. & Kamble, R. R. Chapter 1 - Polymer Synthesis and Processing. in *Natural and Synthetic Biomedical Polymers* (eds. Kumbar, S. G., Laurencin, C. T. & Deng, M.) 1–31 Elsevier, (2014).

132. Armstrong, C. T., Mason, P. E., Anderson, J. L. R. & Dempsey, C. E. Arginine side chain interactions and the role of arginine as a gating charge carrier in voltage sensitive ion channels. *Sci. Rep.* **6**, 21759 (2016).

133. Fitch, C. A., Platzer, G., Okon, M., Garcia-Moreno E, B. & McIntosh, L. P. Arginine: Its pKa value revisited. *Protein Sci. Publ. Protein Soc.* **24**, 752–761 (2015).

134. Liu, S., He, K., Wu, X., Luo, X. & Li, B. Surface modification of cellulose scaffold with polypyrrole for the fabrication of flexible supercapacitor electrode with enhanced capacitance. *RSC Adv.* **5**, 87266–87276 (2015).

135. Rahaman, M., Aldalbahi, A., Almoiqli, M. & Alzahly, S. Chemical and Electrochemical Synthesis of Polypyrrole Using Carrageenan as a Dopant: Polypyrrole/Multi-Walled Carbon Nanotube Nanocomposites. *Polymers* **10**, (2018).

136. Chen, X., Yu, N., Zhang, L., Liu, Z., Wang, Z. & Chen, Z. Synthesis of polypyrrole nanoparticles for constructing full-polymer UV/NIR-shielding film. *RSC Adv.* **5**, 96888–96895 (2015).

137. Wang, M., Cui, M., Liu, W. & Liu, X. Highly dispersed conductive polypyrrole hydrogels as sensitive sensor for simultaneous determination of ascorbic acid, dopamine and uric acid. *J. Electroanal. Chem.* **832**, 174–181 (2019).

138. Ramesan, M. T. & Santhi, V. Synthesis, characterization, conductivity and sensor application study of polypyrrole/silver doped nickel oxide nanocomposites. *Compos. Interfaces* **25**, 725–741 (2018).

139. Umer, A., Liaqat, F. & Mahmood, A. MoO3 Nanobelts Embedded Polypyrrole/SIS Copolymer Blends for Improved Electro-Mechanical Dual Applications. *Polymers* **12**, 353 (2020).

140. Ramesh, S., Leen, K. H., Kumutha, K. & Arof, A. K. FTIR studies of PVC/PMMA blend based polymer electrolytes. *Spectrochim. Acta. A. Mol. Biomol. Spectrosc.* **66**, 1237–1242 (2007).

141. Rahali, K., Messaoud, G. B., Kahn, C. J. F., Sanchez-Gonzalez, L., Kaci, M., Cleymand, F., Fleutot, S., Linder, M., Desobry, S. & Arab-Tehrany, E. Synthesis and Characterization of Nanofunctionalized Gelatin Methacrylate Hydrogels. *Int. J. Mol. Sci.* **18**, (2017).

142. Kubovský, I., Kačíková, D. & Kačík, F. Structural Changes of Oak Wood Main Components Caused by Thermal Modification. *Polymers* **12**, 485 (2020).

143. Bober, P., Liu, J., Mikkonen, K. S., Ihalainen, P., Pesonen, M., Plumed-Ferrer, C., von Wright, A., Lindfors, T., Xu, C. & Latonen, R. Biocomposites of Nanofibrillated Cellulose, Polypyrrole, and Silver Nanoparticles with Electroconductive and Antimicrobial Properties. *Biomacromolecules* **15**, 3655–3663 (2014).

144. Johnston, J. H., Moraes, J. & Borrmann, T. Conducting Polymers on Paper Fibres. *Synth. Met.* **153**, 65–68 (2005).

145. Omastová, M., Trchová, M., Pionteck, J., Prokeš, J. & Stejskal, J. Effect of polymerization conditions on the properties of polypyrrole prepared in the presence of sodium bis(2-ethylhexyl) sulfosuccinate. *Synth. Met.* **143**, 153–161 (2004).

146. Chi, C., Li, X., Zhang, Y., Miao, S., Chen, L., Li, L. & Liang, Y. Understanding the effect of freeze-drying on microstructures of starch hydrogels. *Food Hydrocoll.* **101**, 105509 (2020).

147. Loh, Q. L. & Choong, C. Three-Dimensional Scaffolds for Tissue Engineering Applications: Role of Porosity and Pore Size. *Tissue Eng. Part B Rev.* **19**, 485–502 (2013).

148. Zhu, L., Luo, D. & Liu, Y. Effect of the nano/microscale structure of biomaterial scaffolds on bone regeneration. *Int. J. Oral Sci.* **12**, 1–15 (2020).

149. Zhou, J., Chen, J., Sun, H., Qiu, X., Mou, Y., Liu, Z., Zhao, Y., Li, X., Han, Y., Duan, C., Tang, R., Wang, C., Zhong, W., Liu, J., Luo, Y., Xing, M. & Wang, C. Engineering the heart: Evaluation of conductive nanomaterials for improving implant integration and cardiac function. *Sci. Rep.* **4**, 3733 (2014).

150. Kibrom, A., Roskamp, R. F., Jonas, U., Menges, B., Knoll, W., Paulsen, H. and Naumann, R. L. C. Hydrogel-supported protein-tethered bilayer lipid membranes: a new approach toward polymer-supported lipid membranes. *Soft Matter* **7**, 237–246 (2010).

151. Mawad, D., Artzy-Schnirman, A., Tonkin, J., Ramos, J., Inal, S., Mahat, M. M., Darwish, N., Zwi-Dantsis, L., Malliaras, G. G., Gooding, J. J., Lauto, A. & Stevens, M. M. Electroconductive Hydrogel Based on Functional Poly(Ethylenedioxy Thiophene). *Chem. Mater.* **28**, 6080–6088 (2016).

152. Green, R. A., Lovell, N. H., Wallace, G. G. & Poole-Warren, L. A. Conducting polymers for neural interfaces: Challenges in developing an effective long-term implant. *Biomaterials* **29**, 3393–3399 (2008).

153. Sundfors, F., Bobacka, J., Ivaska, A. & Lewenstam, A. Kinetics of electron transfer between Fe(CN)63−/4− and poly(3,4-ethylenedioxythiophene) studied by electrochemical impedance spectroscopy. *Electrochimica Acta* **47**, 2245–2251 (2002).

154. Spencer, A. R., Primbetova, A., Koppes, A. R., Fenniri, H. & Annabi, N. Electroconductive Gelatin Methacryloyl-PEDOT:PSS Composite Hydrogels: Design, Synthesis, and Properties. *ACS Biomater. Sci. Eng.* **4**, 1558–1567 (2018).

155. Bobacka, J., Lewenstam, A. & Ivaska, A. Electrochemical impedance spectroscopy of oxidized poly(3,4-ethylenedioxythiophene) film electrodes in aqueous solutions. *J. Electroanal. Chem.* **489**, 17–27 (2000).

156. Bobacka, J. Potential Stability of All-Solid-State Ion-Selective Electrodes Using Conducting Polymers as Ion-to-Electron Transducers. *Anal. Chem.* **71**, 4932–4937 (1999).

157. Day, N. U., Walter, M. G. & Wamser, C. C. Preparations and Electrochemical Characterizations of Conductive Porphyrin Polymers. *J. Phys. Chem. C* **119**, 17378–17388 (2015).

158. Charoen-amornkitt, P., Suzuki, T. & Tsushima, S. Ohmic resistance and constant phase element effects on cyclic voltammograms using a combined model of mass transport and equivalent circuits. *Electrochimica Acta* **258**, 433–441 (2017).

159. Mech-Dorosz, A., Khan, M. S., Mateiu, R. V., Hélix-Nielsen, C., Emnéus, J. & Heiskanen, A. Impedance characterization of biocompatible hydrogel suitable for biomimetic lipid membrane applications. *Electrochimica Acta* **373**, 137917 (2021).

160. Vorotyntsev, M. A., Deslouis, C., Musiani, M. M., Tribollet, B. & Aoki, K. Transport across an electroactive polymer film in contact with media allowing both ionic and electronic interfacial exchange. *Electrochimica Acta* **44**, 2105–2115 (1999).

161. Bhat, A., Smith, B., Dinu, C.-Z. & Guiseppi-Elie, A. Molecular engineering of poly(HEMA-co-PEGMA)-based hydrogels: Role of minor AEMA and DMAEMA inclusion. *Mater. Sci. Eng. C* **98**, 89–100 (2019).

162. Temmer, R., Kiefer, R., Aabloo, A. & Tamm, T. Direct chemical synthesis of pristine polypyrrole hydrogels and their derived aerogels for high power density energy storage applications. *J. Mater. Chem. A* **1**, 15216–15219 (2013).

12. APPENDICES

APPENDIX A

Zeta-potential and DLS values of the CNC/PVP/PPy composites prepared with method 1

Zeta-potential (mV)		
	CNC/PVP/PPy	Pristine CNC
Replicate 1	-5.6	-60.80
Replicate 2	-6.2	-68.10
Replicate 3	-5.9	-65.70
Replicate 4	-5.6	-69.10
Replicate 5	-6.8	-71.30
Average	-6.0	-67.0
SD	0.5	4.0

Z-average Size (d. nm)		
	CNC/PVP/PPy	Pristine CNC
Replicate 1	5508	81.8
Replicate 2	5360	79.4
Replicate 3	4372	94.2
Replicate 4	4240	83.9
Replicate 5	4752	84.9
Average	4846	85
SD	600	6

APPENDIX B

Zeta-potential and DLS values of the CNC/PVP/PPy/GelMA hydrogel inks prepared with method 2

	Zeta-potential (mV)					
	GelMA-H-1	GelMA-H-2	GelMA-H-3	GelMA-H-4	GelMA-H-5	Pristine CNC
Replicate 1	2.47	-1.08	5.90	6.20	7.51	-60.80
Replicate 2	2.24	-1.14	6.54	6.98	7.83	-68.10
Replicate 3	2.30	-1.16	6.23	7.35	7.52	-65.70
Replicate 4	2.04	-0.92	5.98	6.50	7.23	-69.10
Replicate 5	2.25	-0.67	6.14	7.00	7.43	-71.30
Average	2.26	-0.99	6.16	6.81	7.50	-67.0
SD	0.14	0.21	0.25	0.45	0.22	4.0

	Z-average Size (d. nm)					
	GelMA-H-1	GelMA-H-2	GelMA-H-3	GelMA-H-4	GelMA-H-5	Pristine CNC
Replicate 1	2857	3752	2759	2087	5903	81.8
Replicate 2	3405	8521	3281	1668	5534	79.4
Replicate 3	6019	13110	3205	1970	6193	94.2
Replicate 4	5750	10170	3150	2241	6026	83.9
Replicate 5	5880	3591	3170	1546	6951	84.9

Average	4782	7828	3113	1902	6121	85
SD	1400	3700	180	260	500	6

APPENDIX C

Zeta-potential and DLS values of the CNC/PPy composites prepared with method 3

	Zeta-potential (mV)						
	CNC/PPy-1	CNC/PPy-2	CNC/PPy-3	CNC/PPy-4	CNC/PPy-5	CNC/PPy-6	Pristine-CNC
Replicate 1	-12.10	-23.50	-31.20	-38.10	-41.20	-34.20	-60.80
Replicate 2	-11.60	-23.50	-33.10	-37.00	-40.60	-36.90	-68.10
Replicate 3	-11.50	-21.50	-32.90	-38.30	-41.10	-36.80	-65.70
Replicate 4	-11.20	-22.20	-31.10	-38.60	-40.60	-34.68	-69.10
Replicate 5	-11.60	-23.80	-31.30	-37.50	-40.30	-34.00	-71.30
Average	-11.60	-22.9	-31.9	-37.9	-40.76	-35.3	-67.0
SD	0.30	1.0	1.0	0.6	0.38	1.4	4.0

	Z-average Size (d. nm)						
	CNC/PPy-1	CNC/PPy-2	CNC/PPy-3	CNC/PPy-4	CNC/PPy-5	CNC/PPy-6	Pristine-CNC

Replicate 1	4365.0	6723.0	2780.0	965.7	1101.0	1076.0	81.8
Replicate 2	4549.0	6167.0	2743.0	963.4	1104.0	1036.0	79.4
Replicate 3	4566.0	6522.0	2930.0	1004.0	1121.0	1061.0	94.2
Replicate 4	4295.0	5405.0	2797.0	975.8	1106.0	1069.0	83.9
Replicate 5	4259.0	4868.0	3074.0	1000.0	1104.0	1095.0	84.9
Average	4407	5937	2865	982	1107	1067	85
SD	140	800	140	19	8	22	6

APPENDIX D

Cyclic voltammograms of the CNC/PPy-3/GGMMA hydrogel, recorded in 0.5 M KCl solution at a scan rate of 10 mV/s.

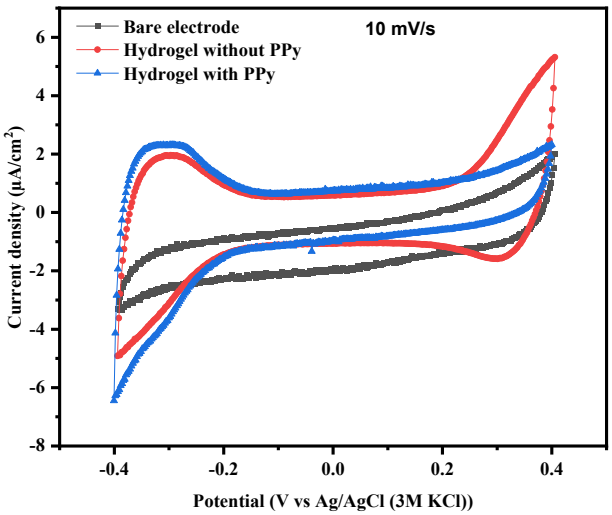

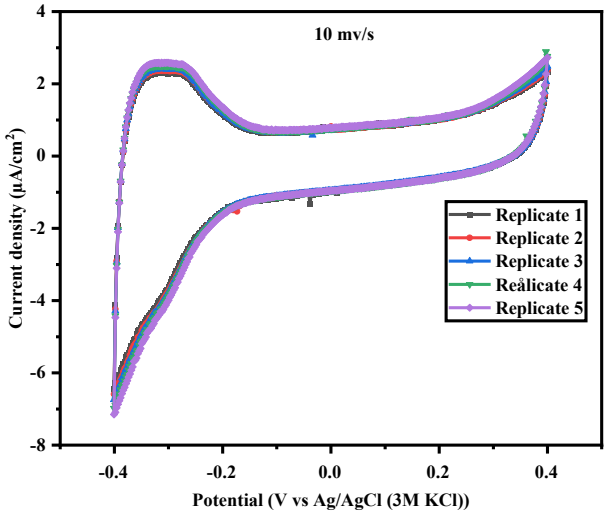

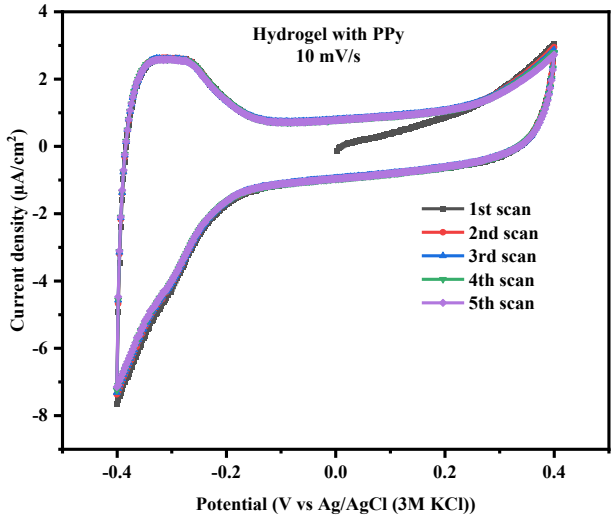

Cyclic voltammogram of the CNC/PPy-3/GGMMA hydrogel, recorded in 0.5 M KCl solution at a scan rate of 20 mV/s

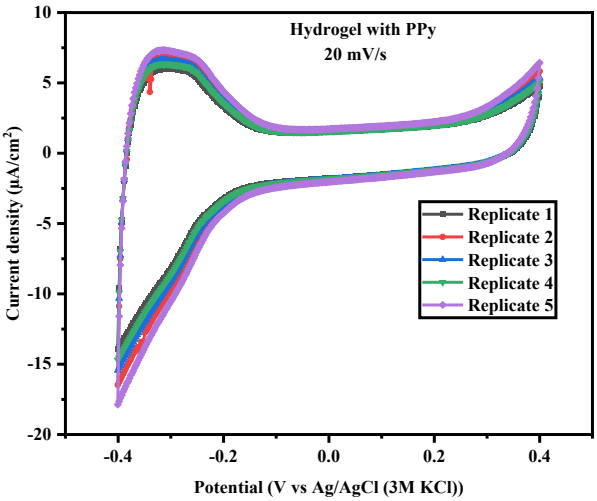

APPENDIX E

Nyquist and Bode plots of the CNC/GGMMA hydrogel that were recorded in 0.5 M KCl solution at E_{ac} = 10 mV; E_{dc} = 0 V and Frequency range = 0.1 Hz to 100 kHz.

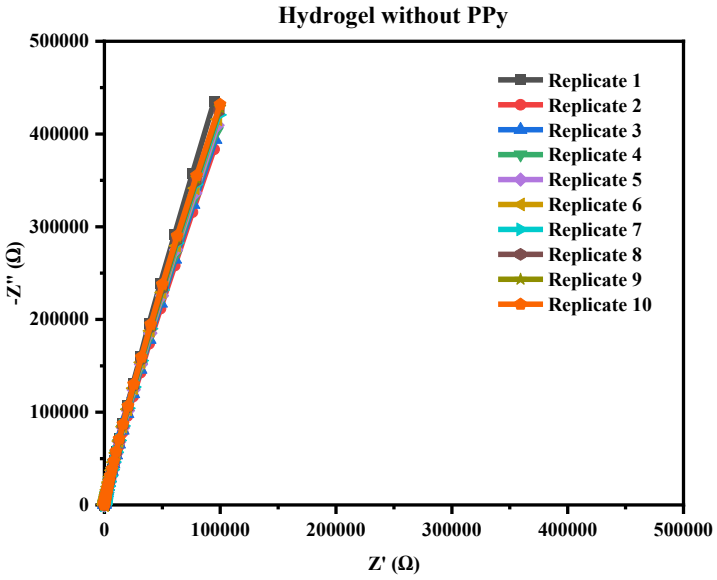

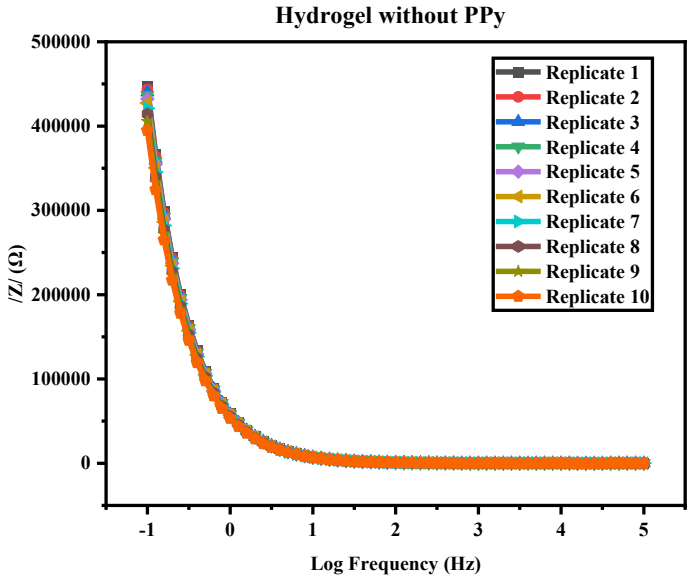

Bode and Nyquist plots of the CNC/PPy-3/GGMMA hydrogel that were recorded in 0.5 M KCl solution at E_{ac} = 10 mV; E_{dc} = 0 V and Frequency range = 0.1 Hz to 100 kHz.

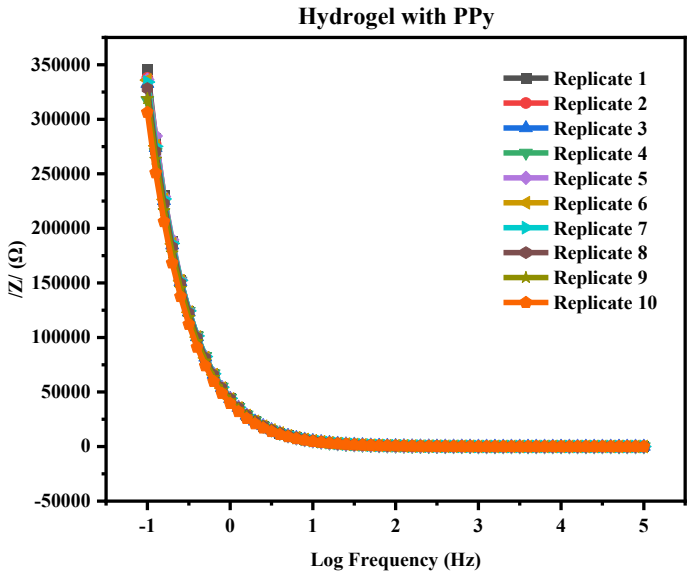

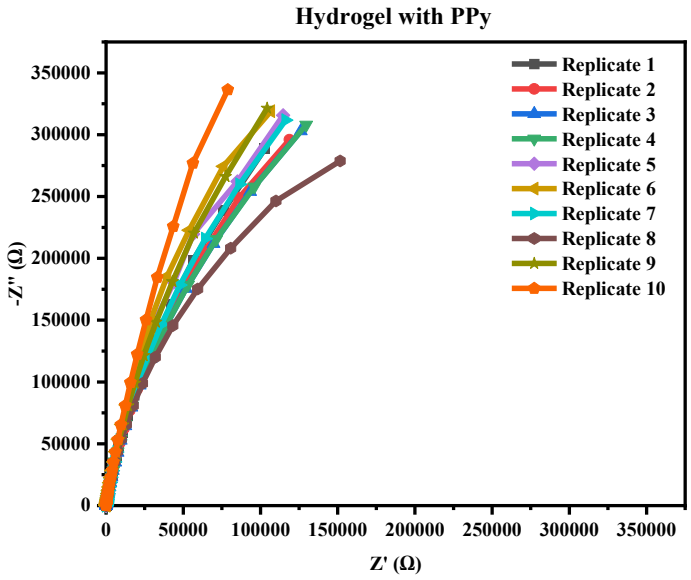

APPENDIX F

Values of the ohmic resistance (R), and the magnitude of $1/Z_{CPE}$ (Q_0), obtained after fitting the EIS spectra to the electrical equivalent circuit in Figure 25.

	R (Ω)		Q_0 (Ss^{α})	
	Hydrogel with PPy	Hydrogel without PPy	Hydrogel with PPy	Hydrogel without PPy
Replicate 1	34.2	33.3	4.87	3.24
Replicate 2	32.6	33.4	4.34	3.26
Replicate 3	32.9	33.4	4.24	3.29
Replicate 4	32.7	33.2	4.3	3.32
Replicate 5	34.1	33.5	4.59	3.35
Replicate 6	34	33.6	4.44	3.39
Replicate 7	34	33.7	4.36	3.44
Replicate 8	33	33.7	4.26	3.5
Replicate 9	32.7	33.8	4.4	3.57
Replicate 10	33.9	33.8	4.36	3.67
Average	33.4	33.54	4.42	3.40
SD	0.7	0.21	0.19	0.14

APPENDIX G

Values of the dispersion coefficient (α) obtained after fitting the EIS spectra to the electrical equivalent circuit in Figure 25.

	α	
	Hydrogel with PPy	Hydrogel without PPy
Replicate 1	0.913	0.909
Replicate 2	0.923	0.909
Replicate 3	0.928	0.908
Replicate 4	0.925	0.907
Replicate 5	0.913	0.906
Replicate 6	0.914	0.905
Replicate 7	0.916	0.903
Replicate 8	0.921	0.902
Replicate 9	0.926	0.9
Replicate 10	0.919	0.898
Average	0.920	0.9047
SD	0.006	0.0038

APPENDIX H

Values of the magnitude of impedance (|*Z*|) at 1 Hz and 1000 Hz were obtained after the EIS measurements in 0.5 M KCl solution at E_{ac} = 10 mV; E_{dc} = 0 V and frequency range = 0.1 Hz to 100 kHz.

	1 Hz		1000 Hz	
	Hydrogel with PPy (Ω)	Hydrogel without PPy (Ω)	Hydrogel with PPy (Ω)	Hydrogel without PPy (Ω)
Replicate 1	39500.62	58947.07	77.68758	113.6315
Replicate 2	42062.64	58647.82	77.92057	113.7491
Replicate 3	43627.34	58312.35	77.91347	113.7945
Replicate 4	44256.96	57891.78	79.12683	113.8102
Replicate 5	43511.03	57778.36	78.29805	113.7631
Replicate 6	44026.33	57124.12	83.23071	113.6285
Replicate 7	43786.87	56431.3	83.09483	113.4455
Replicate 8	44468.94	55573.82	81.8468	113.1386
Replicate 9	43832.54	54619.82	79.27319	112.666
Replicate 10	43819.72	53320.76	80.94244	112.0179
Average	43289	56864	79.9	113.4
SD	1500	1900	2.2	0.6